IMAGING AND AVERAGING IN COMPLEX MEDIA

ROEL SNIEDER
Dept. of Geophysics
Utrecht University
P.O. Box 80.021
3508 TA Utrecht
The Netherlands
email snieder@geo.uu.nl

1. Introduction, complex wave propagation in the earth

Media can be complex in at least two different ways. The first kind of complexity is that a medium has small-scale inhomogeneities that allow waves to travel along a multitude of paths. For such a medium geometrical optics cannot be used to account for the wave propagation. The second kind of complexity is that the inhomogeneities are so strong that multiple scattering effects are operative. In this work the effects of both small-scale perturbations of the medium are treated (section 3), as well as the effects of multiple scattering (section 4). Imaging of wave-fields is very different in complex media than in simple media. The effects of complex wave propagation on imaging techniques is discussed in the sections 2 and 5.

One does not have to look far for a complex medium, because the propagation of elastic waves through the earth can be extremely complex. As an example, consider the top panel of figure 1 in which the ground motion recorded by a seismic station in the Netherlands after an earthquake in Greece is shown. The signal has a very complex appearance. The frequency spectrum of the recorded signal is shown in figure 2. At a frequency of around $0.2Hz$ (corresponding to a period of $5s$) the spectrum shows a pronounced peak. This peak is also present in the absence of waves generated by earthquakes. Instead of the earth response to the earthquake, this peak is due to seismic noise that is generated at the oceans when water waves with

[0]Reprinted from "Diffuse waves in complex media", p. 405-454, Ed. *J.P. Fouque*, Kluwer, Dordrecht, 1999.

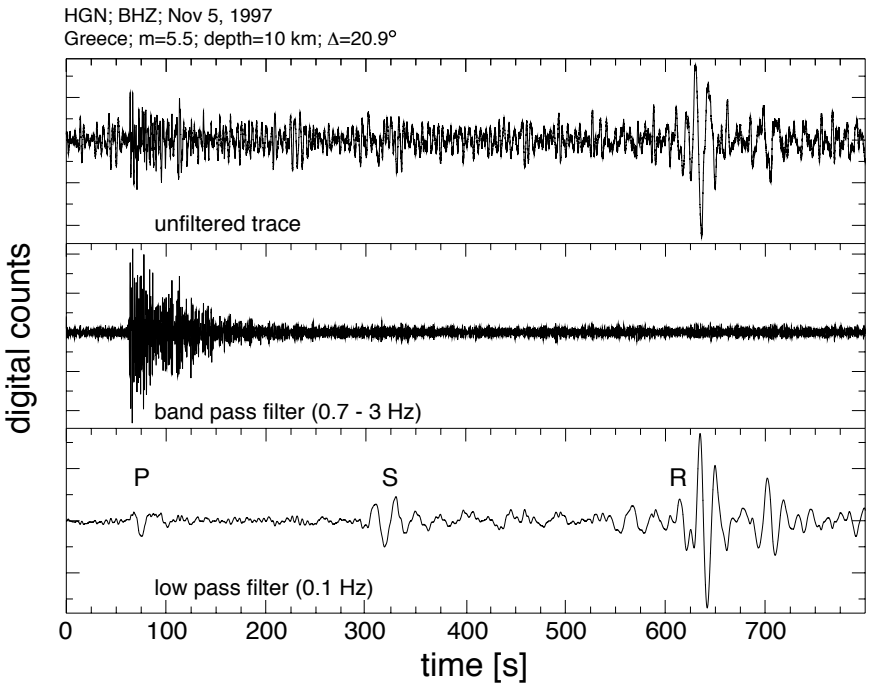

Figure 1. Vertical ground motion recorded in the Netherlands after an earthquake in Greece (top panel). Also shown are the band-passed filtered seismogram containing frequencies from 0.7 Hz to 3 Hz (middle panel) and the low-passed filtered seismogram with frequencies less than 0.1 Hz (bottom panel).

near-opposite wavenumber interact [*Longuet-Higgins,* 1950; *Webb,* 1998]. It turns out that the seismic signal at frequencies greater than the frequency of the microseismic noise is of a completely different character than the signal at lower frequencies.

This can be seen by comparing the seismic signal that contains only frequency components between 0.7 and 3.0 Hz in the middle panel of figure 1 with the low-pass filtered seismogram in the bottom panel of figure 1 that contains only frequencies lower than 0.1 Hz. The high-frequency signal shown in the middle panel starts with an impulsive arrival that directly merges is a long wave-train that consists of multiple scattered waves, this wave-train is called the *coda.*[1] The high-frequency signal shown in the middle panel in figure 1 is of a completely different nature from the low-frequency components shown in the bottom panel. The low-frequency signal does not show a strong coda after the first arriving wave around

[1]The term coda comes from music, where it refers to the closing part of a piece of music.

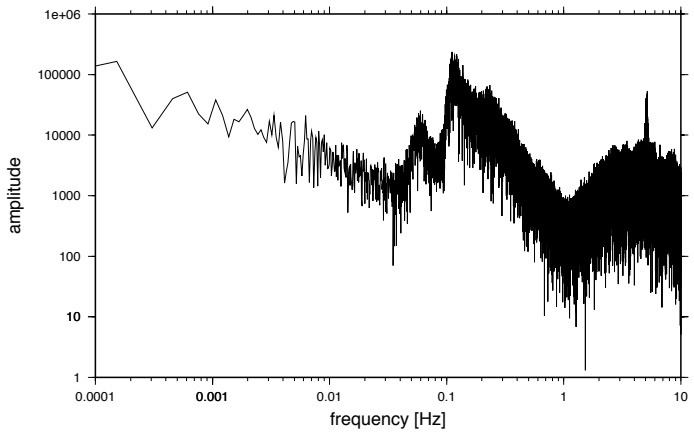

Figure 2. The amplitude spectrum of the seismogram in the top panel of the previous figure.

90s. The main features in this signal are distinct arrivals that correspond to the longitudinal and transverse waves that propagate through an elastic medium. These arrivals are labelled with "P" and "S" according to the common seismological nomenclature of P(rimary)- and S(econdary)-waves. The other main arrival is the surface wave that arrives around 640s after the earthquake, this wave is denoted by the label "R."

It is striking that the frequency-band of the microseismic noise separates for this epicentral distance a wave regime that is dominated by strong scattering (the middle panel) from a regime (in the lower panel) where there is little scattering and where one essentially only observes the direct waves that are explained well by geometrical optics. The waves in both frequency bands travelled through the same medium, the earth. The lesson to be learned from this is that one cannot simply speak of complex media or simple media, because depending on the frequency, the waves may interact in very different ways with the medium. This is due to the frequency-dependence of the relevant scattering and mode-conversion coefficients for body waves [*Aki and Richards*, 1980], surface waves [*Snieder*, 1986; *Snieder and Nolet*, 1987] and for normal modes [*Woodhouse and Dahlen*, 1978; *Snieder and Romanowicz*, 1988]. The name *complex media* is therefore is misnomer, because depending on the frequency the wave propagation in a medium can either be very simple or extremely complex.

On a smaller scale, the material comprising the earth's crust can lead to very complex wave propagation. This is beautifully illustrated by the laboratory measurements made by *Nishizawa et al.* [1997]. Using a laser-doppler interferometer they measured elastic waves that propagate through samples made of granite and of steel. Cross-sections of the three granites that were

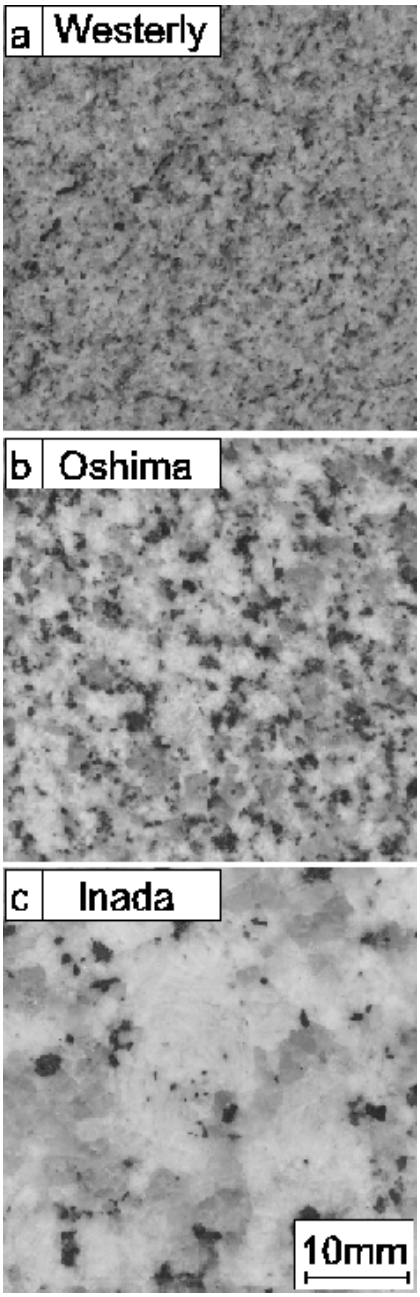

Figure 3. Cross section through the granite samples used for the wavefield measurements shown in the next figures. (Courtesy of Osamu Nishizaza)

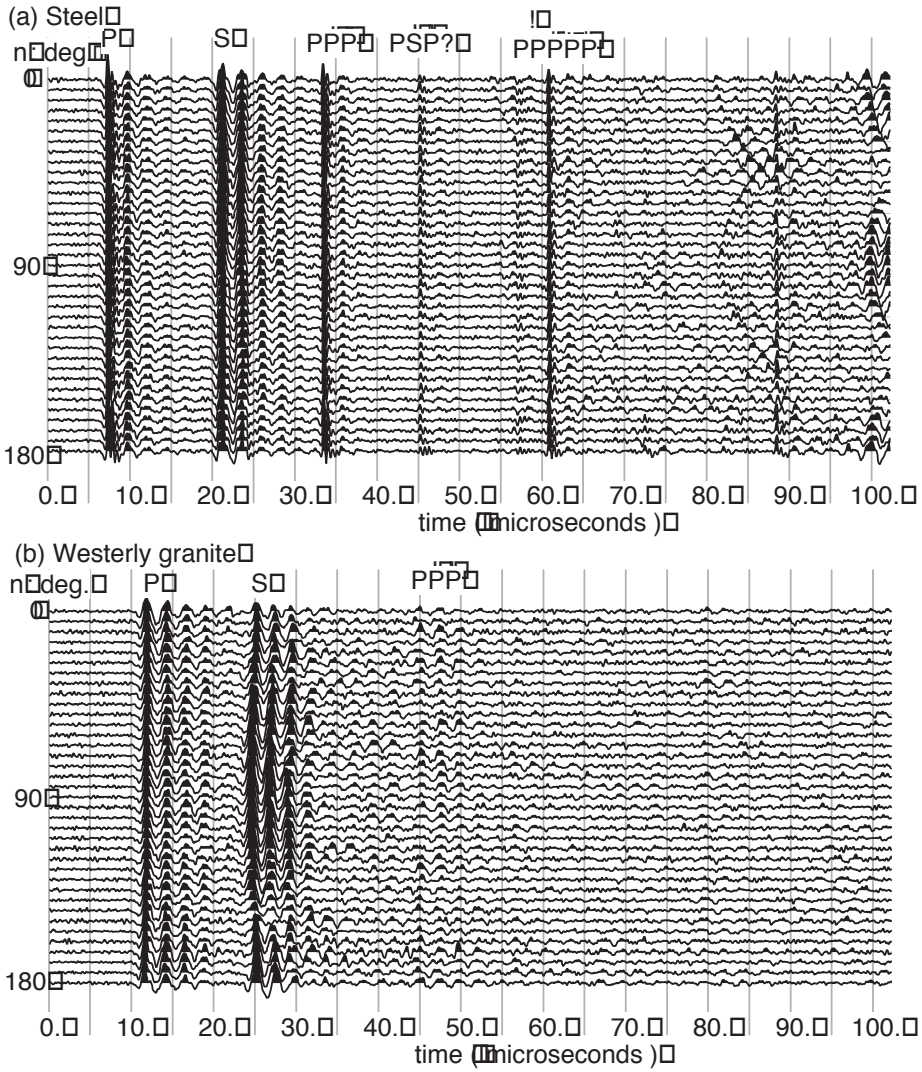

Figure 4. Wavefield that have propagated through a steel block and the Westerley granite sample of the previous figure. (Courtesy of Osamu Nishizawa.)

used are shown in figure 3. The waves that have propagated through these granite samples are shown in the figures 4 and 5. As a reference, the waves that propagated through a steel block is shown in figure 4; the steel block can be considered to be a nearly homogeneous medium. Note that in the steel sample (figure 4) the wave-field is dominated by coherent arrivals that are the P- and S-waves that propagate through the sample and are reflected and converted at the boundaries of the sample. In the most homogeneous

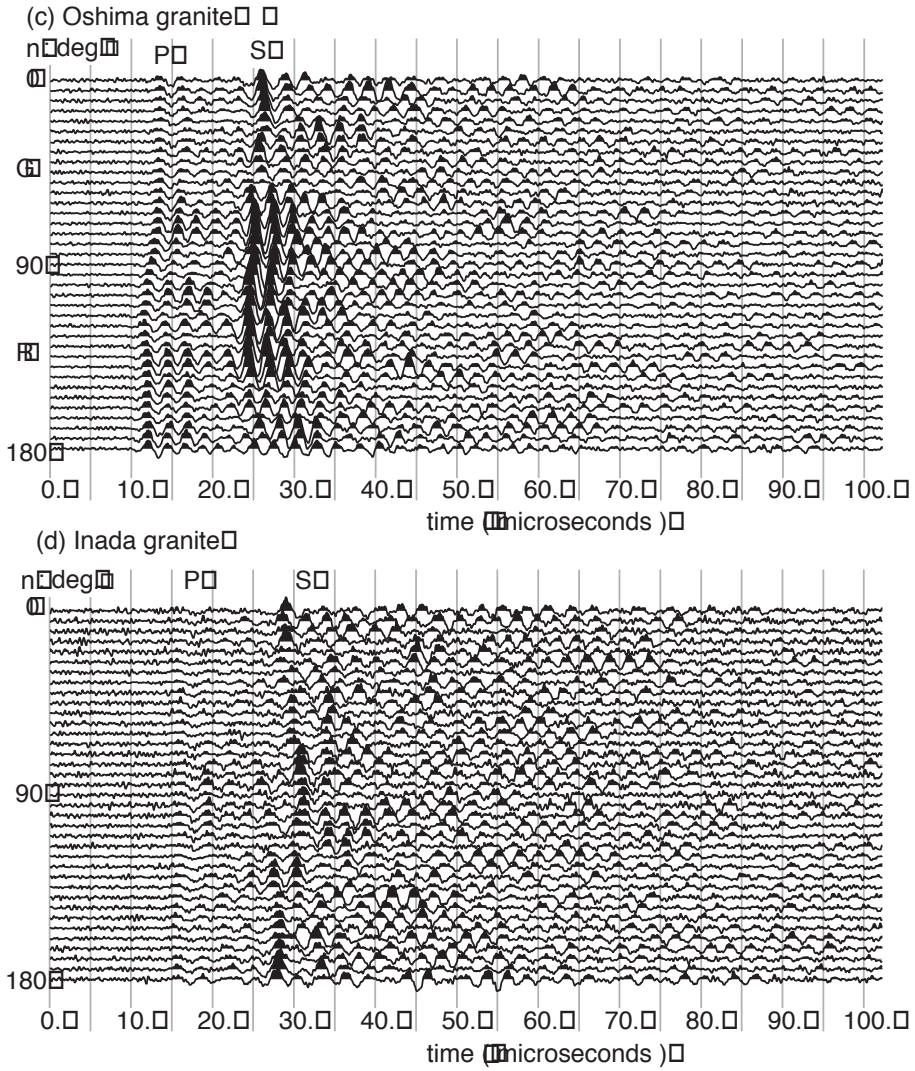

Figure 5. Wavefield that have propagated through the Oshima and Inada granite samples. (Courtesy of Osamu Nishizawa.)

granite sample, the Westerey granite, one can still observe the direct P- and S-waves. However, in the more inhomogeneous granite, notably the Inada granite in figure 5, one cannot identify these direct wave arrivals anymore, and the wave-field makes an incoherent and noisy impression. In this sample the wave scattering is so strong that the direct ballistic arrivals have disappeared.

It is tempting to speak of "noisy signals." However, one should be care-

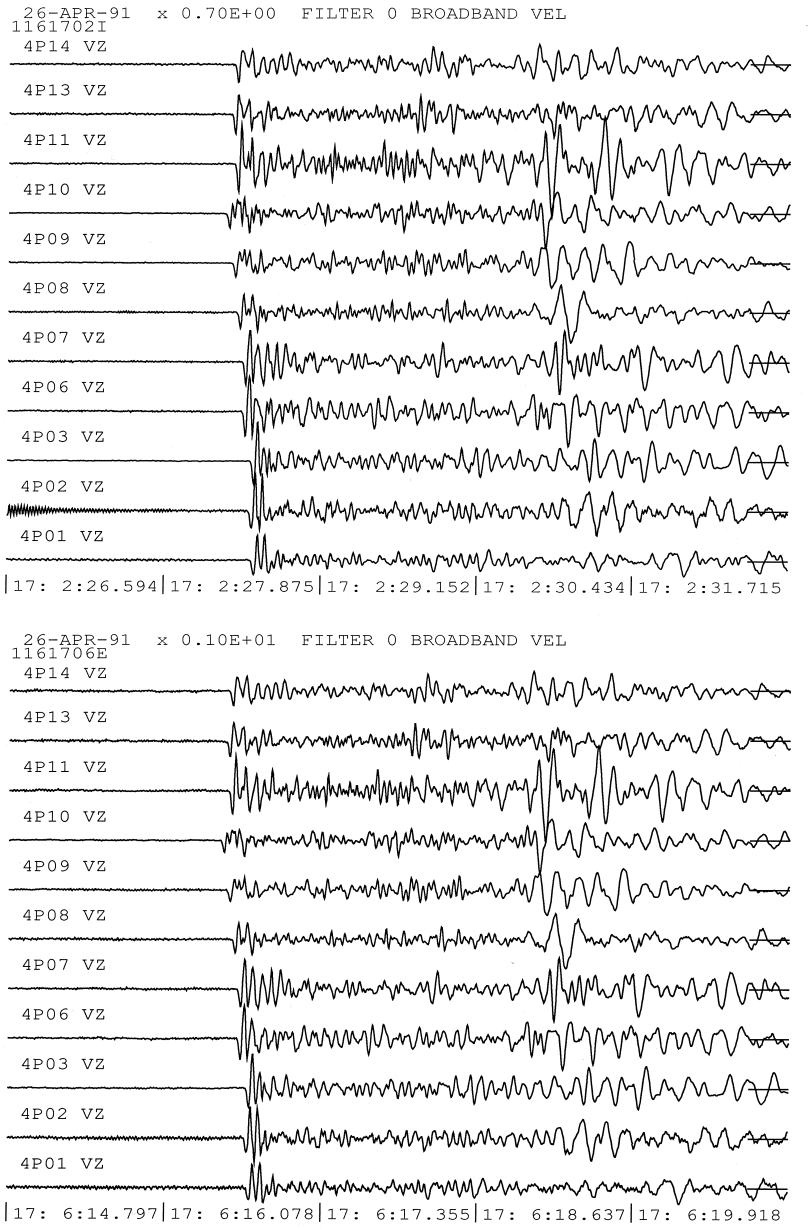

Figure 6. Wave-field recorded by an array in California after two nearby earthquakes (top panel and bottom panel respectively). Note the extreme resemblance of each trace in the top panel with the corresponding trace in the bottom panel. (Courtesy of Peggy Hellweg.)

ful of using the phrase "noise" when referring to wave-fields that appear to show little organisation [*Scales and Snieder*, 1998]. This is illustrated by the recordings of the ground motion of an array in California that is shown in the top panel of figure 6. This ground motion was excited by a weak local earthquake, and the wave propagated mainly through the earth's crust. Note that the wave-field is extremely complex and makes a "noisy" impression because there is little coherence between the signals recorded at different stations. By a stroke of luck, a second very similar earthquake occurred at almost the same location of the first earthquake, the ground motion for this second event recorded by the same array is shown in the bottom panel of figure 6. Note that the signals shown in the panels in figure 6 are virtually identical. The waveforms for these two earthquakes can be matched "wiggle by wiggle." This means that the signals shown in figure 6 are definitely not noise. Instead these signals represent an extremely reproducible earth-response. That these signals are not due to ambient random noise can be seen by considering the signal before the first arriving wave. This part of the recordings is extremely weak; this indicates that the true noise level is extremely low. The noisy looking signals shown in figure 6 therefore should not be labelled as noise but rather as deterministic earth response.

2. Imaging with complex waves?

The wave-fields shown in figure 6 consist to a large extent of multiple scattered waves. In addition to pure wave scattering, the conversion between P-waves, S-waves and surface waves is an additional physical effect that is responsible for generating the waveforms that are recorded. The question then arises: to what extent can these complex waves be used for imaging the earth's interior? Within the seismological community one tends to avoid these complex waveforms when one wants to make images of the earth's interior. The standard approach to seismic prospecting includes a number of processing steps of the data that are aimed at suppressing the multiple scattered waves. The most important example of techniques used for *multiple suppression* is the normal move out (NMO) correction plus stack [e.g. *Claerbout*, 1985; *Yilmaz*, 1987]. In global seismology one often low-pass filters the data in order to remove the multiple scattered waves. The example of figure 1 shows how effective this approach can be. However, the elimination of the multiple scattered waves by preprocessing of the data entails a loss of information.

The main motivation for accepting this loss of information is that the retrieval of earth structure from multiple scattered waves is assumed to be an inherently unstable process so that random noise or unwarranted

assumptions used in the imaging process magnify under the nonlinear inversion steps needed to map the multiple reflected waves onto a model for the earth's interior. It is for these reasons that *Claerbout* [1985] notes on p. 363 that:

> *"Multiple reflections is a good subject for nuclear physicists, astrophysicists and mathematicians who enter our field. Those who are willing to take up the challenge of trying to carry theory through to industrial practice are rewarded by some humility."*

At this point it is not known whether this pessimistic conclusion about the possibility to use strongly scattered waves is justified.

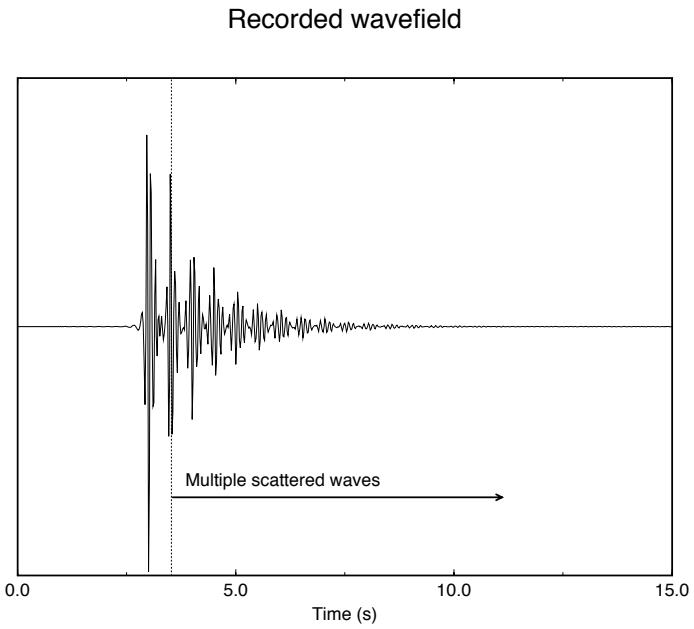

Figure 7. Wave-field at one of the two receivers in the 1D numerical experiment.

In any case, this conclusion appears to be add odds with the experiments of *Derode et al.* [1995] who used a Time Reversal Mirror (TRM) to image acoustic waves that have been strongly scattered back onto the source position. In their experiment, waves emitted by a source propagate through a dense assemblage of 2000 metal rods that strongly scatter acoustic waves. The waves are digitally recorded at an array of 128 receivers. The recorded waves are time-reversed (i.e. the time t is replaced by $-t$) and these time-reversed waves are send back from the receivers into the medium. Since the equation for the propagation of acoustic waves is invariant for time-reversal, the waves should revert along their original path and at time $t = 0$ focus

on the source that originally excited the waves at $t = 0$. The surprise of the experiment of *Derode et al.* [1995] is not that the system exhibits invariance for time reversal, but the surprise is that this time-reversed imaging works even when the employed waves are strongly scattered and when the waves that are send back into the medium are contaminated with errors due to discretization and instrumental effects. The stability of the time-reversed imaging of *Derode et al.* [1995] seems to be at odds with the pessimistic conclusions of *Claerbout* [1985]. So who is right, *Claerbout* [1985] or *Derode et al.* [1995]? Or in other words, can one use multiple scattered waves for imaging purposes or is it impossible to do this in a robust fashion?

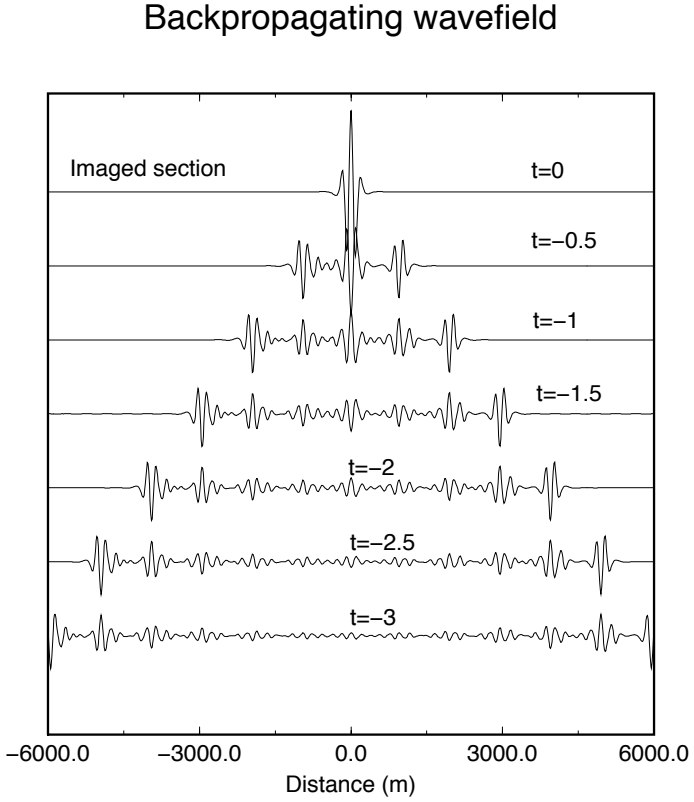

Figure 8. Wave-field after time reversal at different times.

In order to resolve this paradox an example from *Scales and Snieder* [1997] is shown that is based on the multiple scattering theory for isotropic point scatterers that is described in section 4.1. At this point the details of this scattering theory are not yet important, it suffices to note that the full multiple scattering response is used in the numerical simulation. The examples shown are for wave propagation in one dimension, i.e. the waves

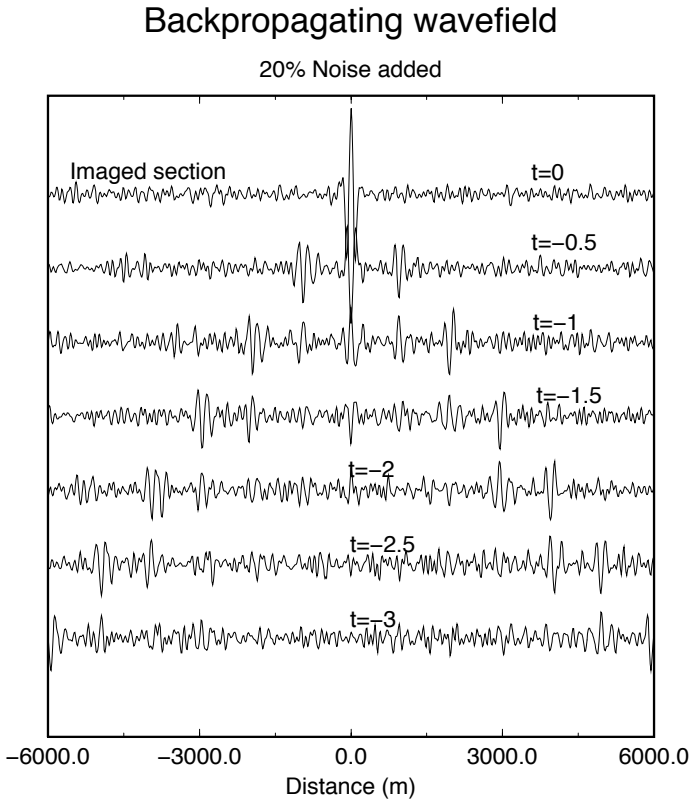

Figure 9. Time-reversed wave-field when 20% noise has been added to the signals that are emitted from the receivers.

propagate along a line. The source is located at $x = 0$, on each side of the source two strong scatterers are positioned within a distance of $500m$. Two receivers located at $\pm 6000m$ record the wave-field. The wave-field recorded by one of the receivers is shown in figure 7. After time-reversal the waves recorded at the two receivers are sent back from the receivers into the medium (which includes the scatterers). In figure 8 one can see how the waves propagate through the medium. Note that the wave-field is confined to a "light-cone" with the source at $x = 0$ and $t = 0$ as apex. As a consequence of the time-reversal invariance of the underlying wave equation, the wave field collapses at $t = 0$ onto the source at $x = 0$.

The time-reversed wave-field for data that are contaminated with 20% noise is shown in figure 9. Despite the background noise in the back-propagating waves, the wave-field still collapses well at $t = 0$ onto the source at $x = 0$. This implies that the back-propagation is fairly stable for the addition of random noise, despite the fact that the waves propagate

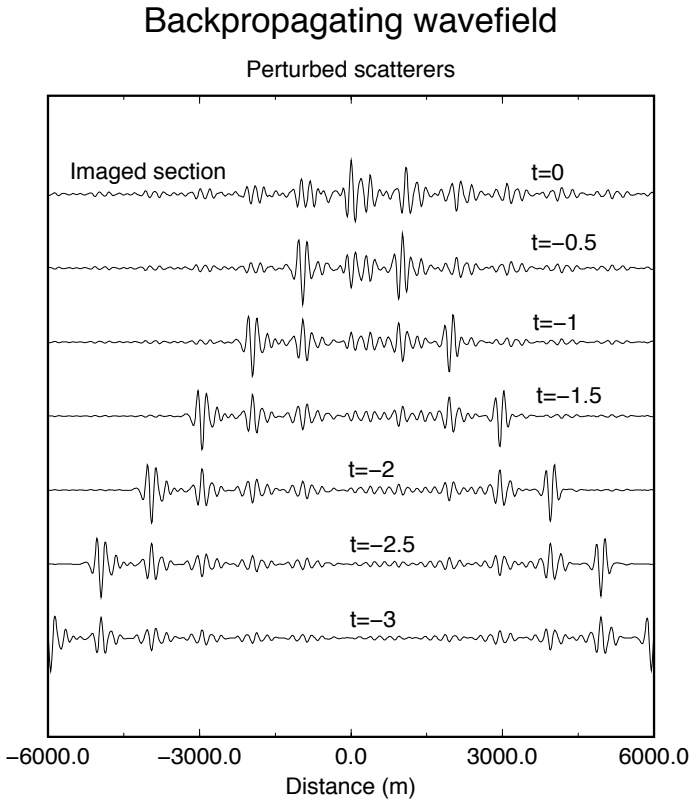

Figure 10. Time-reversed wavefield when the scatterers are perturbed.

through a strongly scattering medium.

Figure 10 shows the time-reversed wave-field propagating through the medium, but now the position of the scatterers have been randomly perturbed with an rms perturbation of about $25m$. (This is $1/4$ of the dominant wavelength.) Note that now the waves poorly focus at $t = 0$ onto the source at $x = 0$ and that energy leaks out off the "light-cone", notably near $t = 0$. The small perturbation in the location of the scatterers has destroyed the delicate interference process that produces the focusing of the wave-field onto the source, which suggests that focusing through multiple scattering media is an inherently unstable process.

Let us now return to the issue: is *Claerbout* [1985] right in his statement about the futility of using multiple scattering data for imaging the earth's interior, or are *Derode et al.* [1995] right with their apparently stable time-reversed experiments? The answer is: both are right! We are considering two different kind of instabilities. In the physical experiment of *Derode et al.* [1995], the time-reversed wave-field is slightly in error because of the 8-bit

digitization that they used. However, the time-reversed wave-field acts as a linear boundary condition on the complete wave-field. This implies that since the medium used by *Derode et al.*[1995] for the forward and reverse propagation is identical, their experiments are not prone to any nonlinear error magnification process. In contrast, *Claerbout* [1985] refers to the fact that imaging is extremely difficult in a strongly scattering medium which is known with only a limited accuracy. His pessimistic conclusion is supported by the example shown in figure 10.

The upshot of this issue is: when one discusses instability of multiple scattering processes one should carefully state whether one refers to (i) instability of the wave-field to perturbations of the boundary conditions, (ii) instability of the wave-field to perturbations of the medium, or (iii) instability of the inverse problem to perturbations of the data. These are different issues that should not be confused.

Note that we have not fully addressed the problem whether imaging of structures is possible on the basis of strongly scattered waves. In fact, this is still an open question. However, strong scattering is not the only complexity seismologists have to deal with. The presence of small-scale structure in the earth imposes an important restriction on the way wave propagation in the earth should be described. The imprint on small-scale variations of the medium on wave propagation is the subject of the next chapter.

3. Averaging in complex media

3.1. RAY THEORY AS WORKHORSE

As shown in the lower panel of figure 1, the elastic response of the earth is for low frequencies characterized by a limited number of wave arrivals. This does not imply that the interior of the earth is a smooth quasi-homogeneous medium. In fact, the coda waves for the high-frequency waves shown in the middle panel of figure 1 show that the interior of the earth is not simple and smooth at all depths. In general, seismologists have followed the strategy to pre-process the data such that the complex wave propagation phenomena are suppressed. The seismic industry relies almost exclusively on single scattered waves for imaging oil reservoirs. Within global seismology, virtually all tomographic models are based on transmission data. Both in seismic imaging and in global seismology one usually employs geometric ray theory to account for wave propagation in the earth. In this sense ray theory can be called the workhorse of seismology.

Ray theory is an approximate theory that is valid when the length-scale a of the inhomogeneity is much larger than:

[1] The wavelength λ of the waves: $a \gg \lambda$

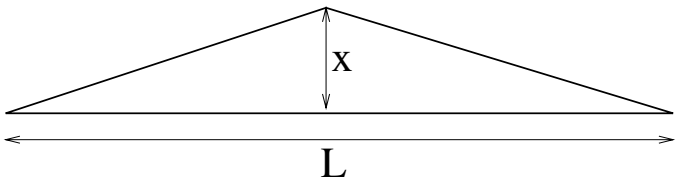

Figure 11. Geometry for the calculation of the Fresnel zone in a homogeneous medium.

[2] The width of the Fresnel zone: $a \gg L_F$

A detailed discussion of these requirements is given by *Kravtsov* [1988].

The definition of the Fresnel zone warrants some further discussion. The (first) Fresnel zone is defined as the region of space that when a wave is scattered once at a point within the Fresnel zone the scattered wave arrives almost in phase with the direct wave. This idea can be based in a more rigorous analysis on Kirchhoff integrals [*Kravtsov,* 1988]. As a first example, consider a homogeneous medium. In such a medium the ray is a straight line. Consider a ray of length L as shown in figure 11, and consider the wave that is scattered once at a point at a distance x from the ray. Let us for simplicity consider a scattering point at the middle of the ray. For small values of x the detour of the scattered wave compared to the direct wave is given by $2\sqrt{(L/2)^2 + x^2} - L \approx 2x^2/L$. When this detour is equal to a quarter of a wavelength one is at the edge of the Fresnel zone. The width of the Fresnel zone is for a homogeneous medium thus given by:

$$L_F = \sqrt{\frac{\lambda L}{8}}\,. \tag{1}$$

One should note that for a fixed wavelength the width of the Fresnel zone grows without limit with the path length L. This means that for a fixed wavelength λ and scale-length a of the heterogeneity the second criterion will always be violated when the path length is of the order of $8a^2/\lambda$.

Let us now consider whether the requirements for the validity of ray theory are satisfied for wave propagation in the earth. As a first example let us consider a P-wave of a period of $1s$ that travels over a teleseismic distance, say $10^4 km$. With a P-velocity of $8km/s$ this leads to a Fresnel zone with a width of $L_F = 100km$. Note that this is really the half-width if the Fresnel zone so that the total width of the Fresnel zone is $200km$. This is about one third of the thickness of the upper mantle, and one may question whether the earth has little variations on that scale.

As a next example consider the Fresnel zone for a PP-wave at the earth's surface that is shown in figure 12. In this example the period of the wave is

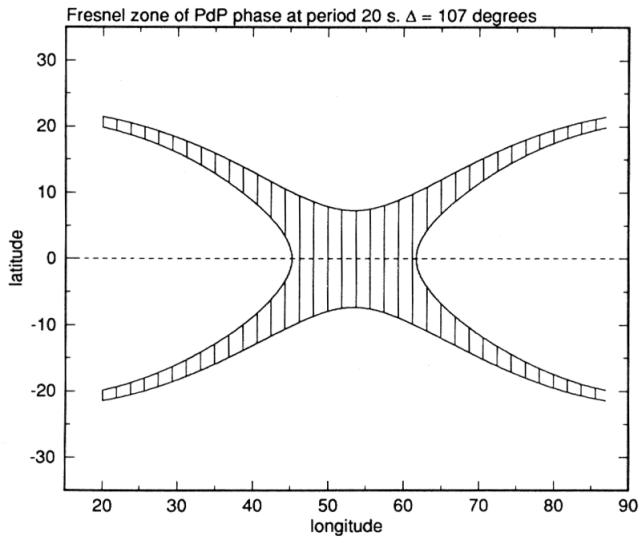

Figure 12. Horizontal cross-section through the Fresnel zone of a PP wave at the bounce point at the Earth's surface for a epicentral distance of 107 degrees and a period of 20s.

$20s$. A PP-wave travels downward from a source, is bend towards the earth's surface, reflects at the earth's surface and then travels to the receiving point. Note that the Fresnel zone for this wave does not have an ellipsoidal cross-section. This is due to the fact that this wave is a minimax phase [*Choy and Richards*, 1975]; this is a different way of saying that the travel time is not a minimum along the ray but that the travel-time surface is a saddle-point surface. However, the important point is not the shape of the Fresnel zone but the size; the total width of the Fresnel zone is about 20 degrees, or about $2000km$. It is not likely that the earth is smooth on this length scale. Other examples of exotic Fresnel zone are shown by *Marquering et al.* [1998].

Fresnel zones can not only be defined for travelling body waves, but also for the normal modes of the earth. Just as an atom with spherical symmetry, a spherically symmetric earth model has normal modes whose horizontal dependence are described by spherical harmonics $Y_{lm}(\theta, \varphi)$. The normal modes with the same order l but different degree m are degenerate and have the same eigen-frequency [*Aki and Richards*, 1980]. One thus has multiplets of normal modes that have a $(2l+1)$-fold degeneracy. Horizontal variations in the earth structure lead to line splitting, and one can show that the centroid-frequency shift $\delta\omega_l$ of a split multiplet observed at a given station for a given earthquake can be written as an integral of the local perturbation δm of the earth's structure [*Tanimoto*, 1984; *Snieder*, 1993;

Dahlen and Tromp, 1998]:

$$\delta\omega_l = \iint K(\theta,\varphi)\delta m(\theta,\varphi)d\Omega \,, \tag{2}$$

where the integration $\iint (\cdots)\, d\Omega$ is over the unit sphere. For the mode ${}_0S_{20}$ with $l = 20$ the weight function $K(\theta,\varphi)$ is shown in figure 13 for an earthquake in Indonesia that is recorded in Western Europe. Positive values are grey, negative values are white. For reference, the great circle joining source and receiver is indicated by a thick line.

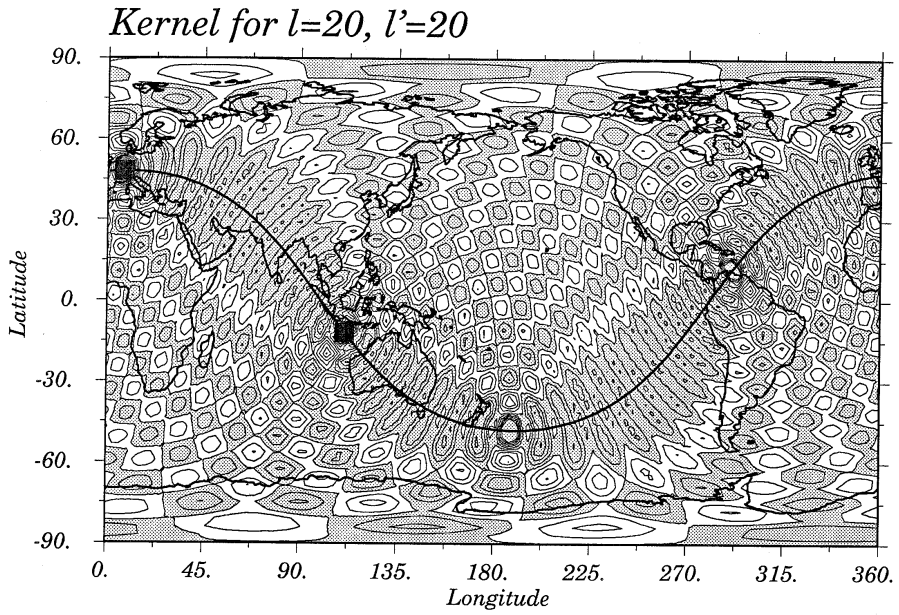

Figure 13. Contour diagram of the sensitivity function $K(\theta,\varphi)$ for mode ${}_0S_{20}$ for an earthquake in Indonesia that is recorded in Europe for mode . Positive values are shown in grey, negative values in white.

Away from the great circle the weight function is oscillatory and changes sign. When the earth structure is smooth on the scale of these oscillations the contribution of this region integrates to zero. The only net contribution then comes from the grey region that straddles the great circle. This region can be seen as the Fresnel zone for this normal mode frequency shift. Note that the width of the Fresnel zone is about $6000km$; the Fresnel zone extends from the north of Tibet to the spreading ridge in the Indian Ocean. It is hard to sustain that the earth structure is smooth on that length scale.

The discussion up to this point assumed that there was a characteristic length-scale of the velocity perturbations in the earth. It is debatable

whether such a length scale indeed exists. In-situ measurements taken in boreholes provide evidence that the structure of the earth's crust is self-similar [*Dolan et al.*, 1998; *Herrmann*, 1997]. Such a medium has perturbations on every length scale, and the criteria for the validity of ray theory are thus surely violated.

The same argument can be used for the propagation of waves through a turbulent medium. Turbulence is characterized by a coupling of the different length-scales of the heterogeneity within the medium by the nonlinear terms in the equation of motion. A turbulent gas or fluid thus displays perturbations on every length scale. This means that ray theory should strictly speaking not be used to describe wave propagation in turbulent media such as the ocean (as used in ocean tomography) or the atmosphere (as used in ionospheric tomography).

It is interesting to consider how we deal with the propagation of light in the atmosphere. We explain the twinkling of the stars using ray theory by stating that thermal fluctuations lead to focussing and defocussing of light that is perceived as twinkling. The argument is ray-geometric. In fact, geometrical optics was originally developed to describe the propagation of light. However, we explain the fact that the sky is blue using scattering theory. In both problems we are considering light of the same wavelength propagating through the same medium but apparently:

At night we believe in ray theory while during the day we believe in scattering theory.

The examples of this section indicate that one often uses ray theory rather carelessly. It is of interest to study the propagation of waves when the requirements for the validity of ray theory are violated. For the moment we will consider media that are complex because they have perturbations on small-scales that violate the requirements for the validity of theory. However, it is assumed in this chapter that the perturbations are weak. For many practical applications such as mantle tomography or light propagation in the atmosphere, this condition is justified. We will return to the issue of wave complexity by multiple scattering by strong perturbations of the medium in section 4.

3.2. PERTURBATIONS OF A HOMOGENEOUS MEDIUM

For simplicity we consider the Helmholtz equation

$$\nabla^2 u + \frac{\omega^2}{v^2(\mathbf{r})}\,(1 + n(\mathbf{r}))\,u = 0\,. \tag{3}$$

The velocity $v(\mathbf{r})$ is a reference velocity that is assumed to be so smooth that ray theory can be used to account for wave propagation through this

medium. The unperturbed wave-field that propagates through this medium is denoted by $u_0(\mathbf{r})$. The velocity is perturbed by the quantity $n(\mathbf{r})$, this quantity is not necessarily smooth. The first order perturbation of the phase of the wave-field follows from the Rytov approximation [*Rytov et al.*, 1989] and is given by

$$\delta\varphi = \Im m\left(\frac{u_B}{u_0}\right) , \tag{4}$$

with u_B given by

$$u_B(\mathbf{r}) = -\int \frac{\omega^2}{v^2(\mathbf{r}')} G(\mathbf{r},\mathbf{r}')n(\mathbf{r}')u_0(\mathbf{r}')dV' , \tag{5}$$

details can be found in *Snieder and Lomax* [1996]. In this expression $G(\mathbf{r},\mathbf{r}')$ is the Green's fucntion for the reference medium $v(\mathbf{r})$.

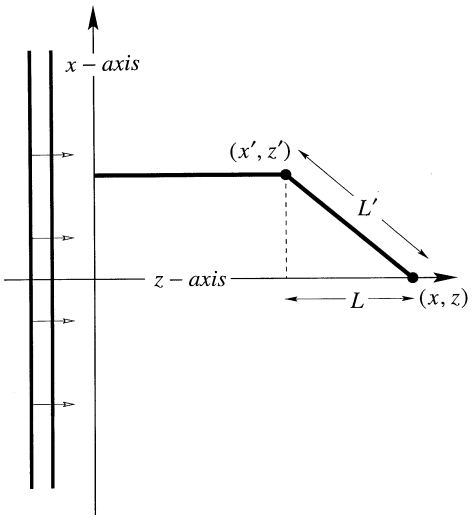

Figure 14. Definition of the geometric variables for a plane incident wave in a homogeneous reference medium.

Let us specialize to the special case of a homogeneous medium in two dimensions with an incoming plane wave that propagates in the z-direction, see figure 14. The wavenumber is given by $k = \omega/v$. The Green's function $G(\mathbf{r},\mathbf{r}')$ in (5) is equal to $(-i/4)\, H_0^{(1)}(k\,|\mathbf{r}-\mathbf{r}'|)$ [*Morse and Ingard,* 1968]. Using the far-field approximation for the Hankel function one can rewrite the phase shift from expressions (4) and (5) as:

$$\delta\varphi(\mathbf{r}) = \Im m\left(\frac{k^2 e^{i\pi/4}}{\sqrt{8\pi k}} \int \left\{ \int \frac{n(\mathbf{r}')e^{ikD(\mathbf{r}')}}{\sqrt{|\mathbf{r}-\mathbf{r}'|}} dx' \right\} dz' \right) . \tag{6}$$

In this expression D is the detour of the scattered wave compared to the direct wave, in the notation of figure 14:

$$D(\mathbf{r}') = L - L' \ . \tag{7}$$

If the perturbation $n(\mathbf{r}')$ would be sufficiently smooth, one could use a stationary phase evaluation of the x'-integral in (6) [*Bleistein*, 1984]. This would lead to the ray-geometric solution [*Snieder,* 1987]. However, the perturbation is not assumed to be smooth, hence the x'-integral cannot be solved with a stationary phase evaluation. Instead, consider the stationary phase integral without the perturbation $n(\mathbf{r}')$ and without the geometrical spreading $\sqrt{|\mathbf{r} - \mathbf{r}'|}$:

$$\int e^{ikD(\mathbf{r}')} dx' = \sqrt{\frac{2\pi \, |z - z'|}{k}} \, e^{i\pi/4} \ . \tag{8}$$

Next, divide the x-integral in (6) by the left hand side of this expression and multiply with the right hand side of (6), and ignoring the variation of the geometrical spreading of $|\mathbf{r} - \mathbf{r}'|$ with x', the result can be written as:

$$\delta\varphi(\mathbf{r}) = \Re e \left(\frac{k}{2} \int \frac{\int n(\mathbf{r}') e^{ikD(\mathbf{r}')} dx'}{\int e^{ikD(\mathbf{r}')} dx'} dz' \right) \ . \tag{9}$$

This is an interesting expression because the x'-integration can be seen as a weigthed average of the perturbation $n(\mathbf{r}')$ with a weight function $\exp(ikD)$. This weight function allows for the relative timing of the scattered waves compared to the direct wave.

When one changes the geometry of the problem the unperturbed wave u_0 changes, and when one considers the problem in 3 dimensions the Green's function changes. This means that for a different geometry the integral (6) has a different form. However, as shown by *Snieder and Lomax* [1996] the averaging integral (9) holds in both 2 and 3 dimensions as well as for a point source instead of a plane incoming wave. The only difference is that in 3 dimensions one needs to integrate over two transverse coordinates x and y. For this reason expression (9) is more general than the original integral (6).

3.3. PERTURBATIONS OF AN INHOMOGENEOUS MEDIUM

The derivation for a homogeneous medium can be generalized for a background medium that is inhomogeneous with velocity variations that are so smooth that it is justified to use ray theory. Perturbations of this medium

are denoted by $n(\mathbf{r})$, these perturbations can have any scale. The corresponding derivation is given by *Snieder and Lomax* [1996] with some corrections in *Snieder and Chapman* [1998]. For such an inhomogeneous reference medium the detour D needs to be replaced by the delay time T of a scattered wave compared to the unperturbed wave. Using ray-centered coordinates [*Červený and Hron,* 1980] the phase shift can for such a medium be written as

$$\delta\varphi = \frac{\omega}{2}\Re e\left(\int ds \frac{1}{v(s)} \frac{\int n(\mathbf{r}) e^{i\omega T} h(s,q_1,q_2) dq_1 dq_2}{\int e^{i\omega T} dq_1 dq_2}\right) . \tag{10}$$

In this expression s is the integration variable along the reference ray while $q_1$and q_2 denote the coordinates perpendicular to the reference ray. The Jacobian of the transformation to ray-centered coordinates is given by $h(s,q_1,q_2) = 1 + (1/v)\,(\mathbf{q}\cdot\boldsymbol{\nabla}\mathbf{v})$. The derivation of (10) is much more complex than the equivalent expression (9) for a homogeneous reference medium because in an inhomogeneous medium the relation between geometrical spreading and wave-front curvature is nontrivial, and one needs to invoke the equations of dynamic ray tracing to derive (10).

However, this expression has a similar interpretation as an averaging integral as (9). The quantity that is averaged in (10) is effectively given by $\omega n(\mathbf{r})/2v(\mathbf{r})$, and the weight function for the function is given by $\exp(i\omega T)$. It follows from the Helmholtz equation (3) that the local wavenumber is given by $k^2(\mathbf{r}) = (\omega^2/v^2(\mathbf{r}))\ \ (1 + n(\mathbf{r}))$. To first order in $n(\mathbf{r})$ the local perturbation of the wavenumber is thus given by

$$\delta k(\mathbf{r}) = \frac{\omega}{v(\mathbf{r})}\left\{\sqrt{1+n(\mathbf{r})} - 1\right\} \approx \frac{\omega n(\mathbf{r})}{2v(\mathbf{r})} \tag{11}$$

This means that according to (10) for a general variable reference medium the phase shift is given by a weighted average of the local wavenumber as defined in (11) with a weight function $\exp(i\omega T)$.

3.4. THE SIGNIFICANCE OF WAVE-FIELD AVERAGING

The equations (9) and (10) state that the perturbation of the phase shift is a weighted average of the slowness perturbation over the Fresnel zone. This implies that the continuity of the wave-field smooths out the perturbations of the medium in the sense that small-scale perturbations of the medium only affect in an average sense the properties of the transmitted wave. As shown in *Snieder and Lomax* [1996] a similar result can be derived for the amplitude of the transmitted wave.

This averaging property plays a crucial role in seismic tomography. As argued in section 3.1 the requirements for the validity of ray theory are

not very justifiable for the earth. Nevertheless, the majority of techniques for seismic tomography are based on ray theory [e.g. *Iyer and Hirahara*, 1993]. Let us now divide the perturbations of the medium in small-scale perturbations that violate the requirements for the validity of ray theory, and large-scale perturbations for which ray theory is valid. The averaging integrals (9) or (10) imply that the small-scale perturbations are averaged out. In contrast, the large-scale perturbations lead to a change in the phase that is identical to the phase shift predicted by ray theory. This means that a tomographic inversion for the large-scale perturbations is not affected by the presence of small-scale perturbations. Only when one aims at resolving features that are smaller than the width of the Fresnel zone, one needs to replace ray theory by the averaging integrals (9) or (10).

Of course, the theory of this chapter is only applicable for perturbations that are so weak that the relation between the perturbation of the phase and the perturbation of the medium can be linearized. However, virtually all schemes for seismic tomography are based on such a linearization, hence this is no additional complexity as far as the application in seismic tomography is concerned.

3.5. FOR THOSE WHO DON'T LIKE THE RYTOV APPROXIMATION

Readers may not feel comfortable with the use of the Rytov approximation. The validity of the Rytov approximation is a topic of heated debate for at least 30 years. An important restriction of the Rytov approximation is that there is no known generalization to vector waves. The results obtained in section 3.2 can, however, also be obtained in a completely different way by making a coordinate transformation as shown in figure 15 from the Cartesian coordinates (x, y, z) to a new coordinate system (x, y, Z) where the lines of constant values of the new Z-coordinate coincide with the perturbed wavefronts [*Snieder*, 1998]. One can view this technique as a higher-dimensional version of the method of strained coordinates [*Nayfeh*, 1973] Solving the wave equation in this new coordinate system using a parabolic approximation leads to the same averaging integral (9) as was obtained from the Rytov approximation.

4. Multiple scattering by isotropic point scatterers

As argued in section 1, complex variations in the structure of the earth can give rise to very complex waveforms through the process of multiple scattering, see the examples in the middle panel of figure 1 and in the figures 6. Formulating a multiple scattering theory for the general elastic problem is a task of formidable proportions. However, for the special case of

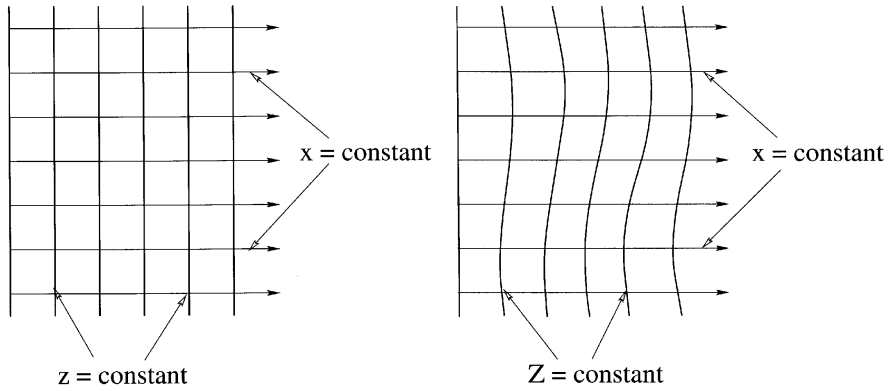

Figure 15. Definition of the coordinate systems (x, y, z) and (x, y, Z) where the planes $z = const$, coincide with the unperturbed wavefront (left panel) and where the planes $Z = const$, coincide with the perturbed wavefront (right panel).

isotropic point scatterers the multiple scattering problem has a very simple and elegant solution.

4.1. DERIVATION OF THE THEORY

Let us consider a system with point scatterers at locations $\mathbf{r}_j$. The complex scattering coefficient of scatterer j is denoted by A_j. This coefficient contains the full nonlinear interaction of the wave that is incident on the scatterer and the scattered wave. It is shown in appendix A that this scattering coefficient contains the superposition of all consecutive multiple scattering interactions with the same scatterer. Let the total wave-field that is incident on scatterer j be denoted by u_j. The wave that is scattered by this scatterer is then given by $G(\mathbf{r}, \mathbf{r}_j)A_j u_j$, where $G(\mathbf{r}, \mathbf{r}')$ is the Green's function for the medium in which the scatterers are embedded. Since the scattering is assumed to be isotropic, there is no dependence on the scattering angle. The total wave-field can be written as the superposition of the unperturbed wave $u^{(0)}(\mathbf{r})$ and the waves emanating from all the scatterers:

$$u(\mathbf{r}) = u^{(0)}(\mathbf{r}) + \sum_j G(\mathbf{r}, \mathbf{r}_j)A_j u_j \,. \tag{12}$$

The wave-field that is incident on scatterer i follows from this expression by setting $\mathbf{r} = \mathbf{r}_i$, and by omitting the term $j = i$ from the sum in (12) because the wave incident wave on scatterer i only has contributions from the unperturbed wave $u^{(0)}(\mathbf{r})$ and from the waves coming from the *other*

scatterers:

$$u_i = \mathbf{u}^{(0)}(\mathbf{r}_i) + \sum_{j \neq i} G(\mathbf{r}_i, \mathbf{r}_j) A_j u_j \ . \tag{13}$$

This is all that is needed to solve the scattering problem. Equation (13) constitutes a linear system of equations for the complex coefficients u_j. This system can be solved numerically. Once the u_j are determined one can compute the wave-field at any location $\mathbf{r}$ by inserting the u_j in expression (12).

For convenience the system of equations (13) can also be written in vector form:

$$(\mathbf{I} - \mathbf{S})\, \mathbf{u} = \mathbf{u}^{(0)} \ , \tag{14}$$

where $\mathbf{u}$ is the vector with u_j as the j-th component and the vector $\mathbf{u}^{(0)}$ has $u^{(0)}(\mathbf{r}_j)$ as the j-th component. The identity matrix is denoted by $\mathbf{I}$ and the components of the matrix $\mathbf{S}$ are given by:

$$S_{ij} = \begin{cases} 0 & for\ i = j \\ G(\mathbf{r}_i, \mathbf{r}_j) A_j & for\ i \neq j \end{cases} \tag{15}$$

When energy is conserved, the optical theorem imposes a constraint on the imaginary component of the forward scattering amplitude and the scattered power averaged over all directions [*van der Hulst*, 1949; *Ishimaru*, 1997]. The generalization of the optical theorem for elastic surface wave modes is given by *Snieder* [1988]. For isotropic scatterers the optical theorem imposes the following constraint on the scattering coefficient in different dimensions:

$$\Im m(A) = \begin{cases} -\dfrac{1}{2k} |A|^2 & in\ 1D \\ -\dfrac{1}{4} |A|^2 & in\ 2D \\ -\dfrac{k}{4\pi} |A|^2 & in\ 3D \end{cases} \tag{16}$$

Note that the scattering formalism can be applied to any number of dimensions and that the numerical implementation is very similar in different number of dimensions.

4.2. THE FEYNMAN PATH SUMMATION

The scattering equations of the previous section can be rewritten in a different form that is useful for a number of applications. The linear system of equations (14) can be solved by matrix inversion: $\mathbf{u} = (\mathbf{I} - \mathbf{S})^{-1}\, \mathbf{u}^{(0)}$. Using

an expansion of the inverse $(\mathbf{I}-\mathbf{S})^{-1}$ this can also be written as:

$$\mathbf{u} = \mathbf{u}^{(0)} + \mathbf{S}\mathbf{u}^{(0)} + \mathbf{S}^2\mathbf{u}^{(0)} + \mathbf{S}^3\mathbf{u}^{(0)} + \cdots \tag{17}$$

Inserting this expression in (12) and using the definition (15) for $\mathbf{S}$, the total wave-field is given by

$$u(\mathbf{r}) = u^{(0)}(\mathbf{r}) + \sum_i G(\mathbf{r},\mathbf{r}_i)A_i u^{(0)}(\mathbf{r}_i) + \sum_{i\neq j}\sum_j G(\mathbf{r},\mathbf{r}_i)A_i G(\mathbf{r}_i,\mathbf{r}_j)A_j u^{(0)}(\mathbf{r}_j) + \ldots \tag{18}$$

This result can be seen as the Neumann series solution of the scattering problem. The series does have a clear physical meaning. The first term denotes the arrival of the unperturbed wave. The second term consists of all the single scattered waves. The second term contains all the waves that are scattered twice by different scatterers. The series (18) can thus be seen as a summation of waves that have travelled along all possible paths between scatterers, *but that never visit the same scatterers on two consecutive scattering events*. One can therefore view expression (18) as a discrete version of the Feynman path integral [*Feynman and Hibbs*, 1965] where the total wave-field is expressed as a path-integral over all possible trajectories. Since (18) is the discrete equivalent of the Feynman path integral it will be called the "Feynman path summation." Note that no approximations have been made in the deriving the Feynman path summation.

With a slight change of notation one can write the Feynman path summation also as

$$u(\mathbf{r}) = \sum_P e^{ikL_P}\,(\Pi C)\,u^{(0)}\ . \tag{19}$$

In this expression the sum $\sum_P$ denotes a sum over all paths starting from the source and travelling along all possible combinations of scatterers with the same scatterer not encountered on consecutive scattering events. The path length for path P is denoted by L_P. The term (ΠC) gives the product of scattering coefficients for that path and the geometrical spreading and other constants that appear in the Green's function. Note that for 2 dimensions, one can only split-off the term $\exp(ikL_P)$ when the distance between the scatterers is much larger than a wavelength so that the far-field approximation for the Hankel function can be used.

4.3. THE EFFECTIVE WAVENUMBER FOR AN ENSEMBLE OF SCATTERERS

Let us consider a medium of isotropic point scatterers as described in section 4.1. The scatterers have three effects: (1) the ballistic wave that travels through the medium will experience a phase shift, (2) the ballistic wave will

be reduced in amplitude due to scattering losses and (3) a coda of scattered waves is generated. In this section we will not account for the last effect. The first two effects can be described by introducing an effective local wavenumber k_{eff} for the medium with the scatterers. This effective wavenumber was derived by *Groenenboom and Snieder* [1995] using an approximate invariant embedding technique. In this section the effective wavenumber is derived using the averaging integral that is derived in section 3.2.

As a starting point consider the Helmholtz equation (3) for the special case that the reference medium is homogeneous:

$$\nabla^2 u(\mathbf{r}) + k^2 \left(1 + n(\mathbf{r})\right) u(\mathbf{r}) = 0 \; . \tag{20}$$

In order to relate this equation to the scattering theory of section 4.1 we need to establish the connection between the perturbation $n(\mathbf{r})$ and the scattering coefficients A_j in (12). This can be achieved by letting the operator $(\nabla^2 + k^2)$ act on (12). Using the fact that the unperturbed wave satisfies $(\nabla^2 + k^2)\, u^{(0)}(\mathbf{r}) = 0$ and that the Green's function satisfies $(\nabla^2 + k^2)\, G(\mathbf{r}, \mathbf{r}') = \delta(\mathbf{r} - \mathbf{r}')$ one finds that

$$\left(\nabla^2 + k^2\right) u(\mathbf{r}) = \sum_j \delta(\mathbf{r} - \mathbf{r}_j) A_j u_j \; . \tag{21}$$

Comparing this with (20) one readily finds that

$$n(\mathbf{r}) = - \frac{1}{k^2} \sum_j \delta(\mathbf{r} - \mathbf{r}_j) A_j \; . \tag{22}$$

In order to obtain an effective wavenumber, let us write the phase change due to the perturbation in equation (9) as $\delta\varphi = \int \delta k \; dz$, where δk is the perturbation in the wavenumber. Inserting (22) in the averaging integral (9) and using the above expression for δk one obtains the following expression for the wavenumber perturbation:

$$\delta k = \frac{1}{2} k \left\langle n \right\rangle_F = - \frac{1}{2k} \left\langle \sum_j \delta(\mathbf{r} - \mathbf{r}_j) A_j \right\rangle_F \; . \tag{23}$$

The brackets $\langle \cdots \rangle_F$ do *not* denote an ensemble average, but a weighted average over the Fresnel zone:

$$\langle \cdots \rangle_F \equiv \frac{\int (\cdots)\, e^{ikD(\mathbf{r}')} dx'}{\int e^{ikD(\mathbf{r}')} dx'} \tag{24}$$

Note that we have tacitly removed the operation of taking the real part of (23). Since the scattering coefficients A_j are complex, the wavenumber

perturbation is also complex. This describes the amplitude decay of the ballistic wave due to scattering losses. One can derive this rigorously by using that the logarithmic perturbation of the amplitude is the imaginary part of the averaging integral in (9), see *Snieder and Lomax* [1996] for details. Adding the wavenumber perturbation δk to the unperturbed wavenumber k one obtains the complex effective wavenumber:

$$k_{eff} = k - \frac{1}{2k} \left\langle \sum_j \delta(\mathbf{r} - \mathbf{r}_j) A_j \right\rangle_F \tag{25}$$

Let us now consider the special case that the scatterers have an identical scattering coefficient A and that the weight function in the averaging integral is replaced by its value on the reference ray: $\exp(ikD) \rightarrow 1$. Under these assumptions the wavenumber perturbation integrated in the z-direction can be rewritten in the following way:

$$\begin{aligned} \int \left\langle \textstyle\sum_j \delta(\mathbf{r} - \mathbf{r}_j) A_j \right\rangle_F dz &= A \int \left\langle \textstyle\sum_j \delta(\mathbf{r} - \mathbf{r}_j) \right\rangle_F dz \\ &= A \, \frac{\text{Number of scatterers in Fresnel zone}}{\text{Volume of Fresnel zone}} \\ &= A \langle N \rangle \end{aligned} \tag{26}$$

where $\langle N \rangle$ is the number of scatterers per unit volume area over the Fresnel zone. The corresponding effective wavenumber is then given by

$$k_{eff} = k - \frac{A \langle N \rangle}{2k} \tag{27}$$

This expression agrees with the effective wavenumber that is derived using other techniques [*Lax*, 1951; *Waterman and Truell*, 1961].

4.4. A NUMERICAL EXAMPLE

As an illustration of the theory of this chapter a numerical example of wave propagation in two dimensions is presented. The geometry of the problem is shown in figure 16. An isotropic source (shown by a square) is placed in the middle of 12 receivers (shown by triangles) that are located on a circle. Between the source and the receivers point scatterers are present, these are indicated by dots. Details on the parameters used in the simulation can be found in *Groenenboom and Snieder* [1995].

The wave-field in the absence of scatterers is indicated by the dashed line in figure 17. Since the source is isotropic and the reference medium is

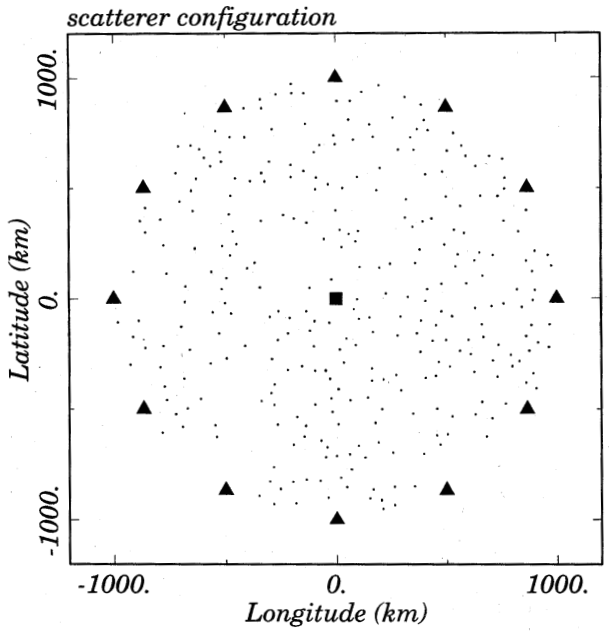

Figure 16. Geometry of the scattering experiment with a source (square) surrounded by 12 receivers (triangles) and scatterers (dots).

homogeneous the unperturbed wave is identical for all the receivers. The exact scattering response is indicated by the thin solid line in figure 17. This response was computed using the expressions (12) and (13) in the frequency domain and by carrying out a Fourier transform. Note that the amplitude of the ballistic wave has been reduced severely (about a factor 3) due to scattering losses. This strong scattering loss is consistent with the presence of strong scattered waves after the arrival of the ballistic wave. This means that in this problem strong multiple scattering is operative.

The thick solid line in figure 17 gives the wave-field computed with the effective wavenumber given in expression (27). For every source-receiver pair this quantity was computed by counting the number of scatterers within the Fresnel zone for that source-receiver pair. Note the good agreement between the ballistic wave in the exact response and the wave-field computed with the effective wavenumber (27). The scattered waves arriving after the ballistic wave are not reproduced in the wave-forms computed with the effective wavenumber technique. This is due to the fact that in this

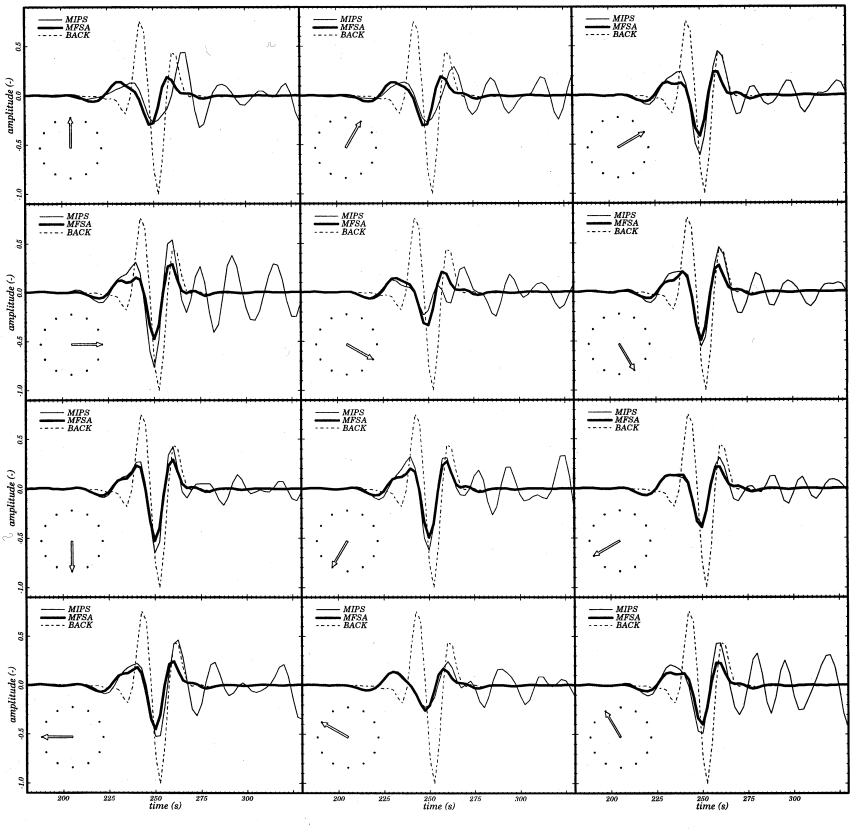

Figure 17. Waves at the 12 receivers of the previous figure. The clock indicates the receiver position. Shown is the wave-field in the absence of scatterers(dashed line), the complete wavefield in the presence of scatterers (thin solid line) and the wavefield computed with the effective wavenumber technique (thick solid line).

approach only the scatterers within the Fresnel are accounted for, whereas the coda is generated by the scatterers outside the Fresnel zone as well.

The ballistic wave varies considerably for the different receivers due the variations in the scatterer density. Notice that the waveforms computed with the effective wavenumber technique follow this variability quite well. It can be seen that the waveforms in the presence of scatterers exhibit a pronounced dispersion that is reproduced well with the effective wavenumber approach. This example shows that the effective wavenumber can be a powerful tool for describing the effects of scattering on the ballistic wave, even in the case when this wave is strongly perturbed.

5. Imaging waves or particles in strongly scattering media

In this section we return to the issue to what extent imaging in strongly scattering media is possible. It was shown in section 2 that the random addition of noise enters only the linear boundary conditions of the problem, hence it does not need to be considered as a source of instability due to nonlinear effects. In classical mechanics, the instability of trajectories of particles to perturbations of the initial conditions is the signature of chaotic behavior [e.g. *Tabor*, 1989]. In order to use waves for imaging purposes, the temporal evolution of the wave-field may or may not be unstable for perturbations of the location of the source of the wave-field or for perturbations of the medium. In this sense one may wonder how the *wave-field* in a strongly scattering system behaves when it is known that *particles* propagating through the same system exhibit chaotic behavior. The imprint of chaos on wave systems is usually studied in the context of quantum chaos [e.g. *Tabor,* 1989; *Gutzwiller,* 1990]. However, in that field of research the attention usually is focused on the spectral properties of a closed wave-system rather than the stability of the temporal evolution of the wave-field.

The issue of the stability of the temporal evolution of wave or particle propagation can be studied using a Time-Reversal-Mirror. This device has been used in laboratory experiments [*Derode et al.,* 1995; *Fink*, 1997]. In this technique wave propagate through a medium and are recorded at receivers. The recorded wave-field is reversed in time, which is equivalent by replacing t by $-t$, and this time-reversed wave-field is send back into the medium. Since the system is invariant for time reversal, the wave propagate back along their original path and focus back on the original source position at $t = 0$. Since the waves are imaged in this method on the original source position this technique will be referred to as Time-Reversed-Imaging (TRI). This principle can obviously also be applied to particles. Whether the waves (or particles) really return to the original source position when the system is perturbed depends on the stability properties of the wave or particle propagation.

The system used here is similar to the one used by *Derode et al.* [1995] and is shown in figure 18. The numerical experiments shown in this section are from *Snieder and Scales* [1998]. Particles or waves are emitted from a source and propagate through a system of 200 strong isotropic point scatterers. For the waves, 96 receivers are located on the line indicated in figure 18. The recorded wave-forms are time-reversed and then send back into the medium from the receivers that now act as sources. A particle is recorded for the time-reversed imaging when it traverses the receiver line in figure 18 at a certain time t. TRI of the particle is realized by reversing

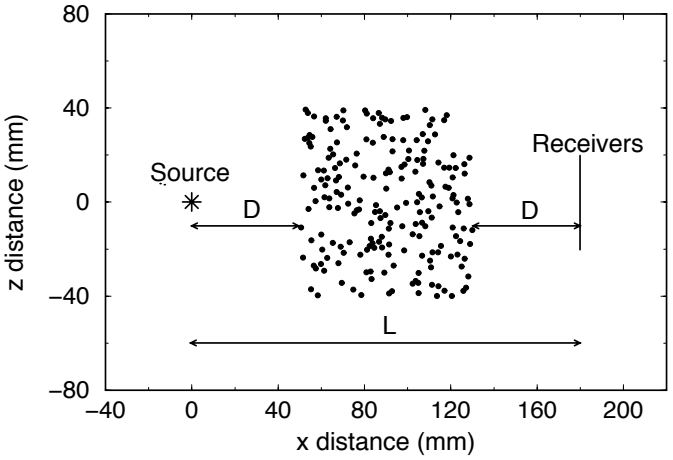

Figure 18. Geometry of the numerical experiment with TRI. The scatterers are shown by thick dots.

the velocity of the particle $\mathbf{v} \rightarrow -\mathbf{v}$ and by sending the particle back into the medium at time $-t$.

When comparing the stability of wave or particle propagation, one can either specify the medium (e.g. a quantum mechanical potential) or the scattering properties of the waves and particles. Here the latter approach is taken by using isotropic point scatterers for both waves and particles. This choice ensures that the only difference between the waves and particles lies in the dynamics of propagation, rather than in a different interaction with the scatterers.

5.1. SCATTERING OF PARTICLES AND WAVES

Isotropic scattering of particles that is invariant under time reversal is ensured by requiring that both the velocity v (*=1500 m/s)* and the impact parameter b of the particles are conserved during scattering and that (in two dimensions) the scattering angle Θ is linear in the impact parameter:

$$\Theta = \pi \left(\frac{\sigma - 2b}{\sigma} \right) \qquad for \quad |b| \leq \sigma/2 \,, \tag{28}$$

where σ is the scattering cross-section. See figure 19 for the definition of variables. For larger values of the impact parameter the particle is not

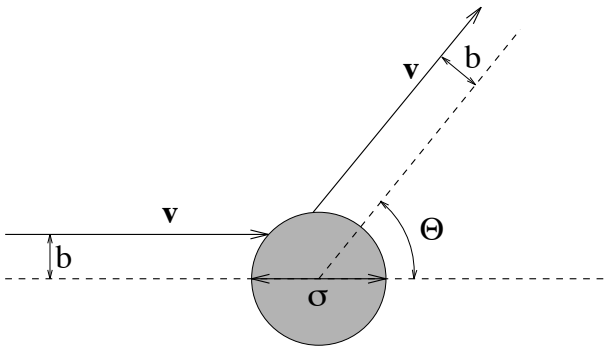

Figure 19. Definition of the impact parameter b and the scattering angle Θ.

scattered (i.e. $\Theta = 0$). Table 1 shows the values of the relevant length

TABLE 1. Numerical values of parameters in the numerical experiment.

Symbol	Property	Value
σ	Scattering cross section	1.592 mm
l	Mean free path	15.56 mm
λ	Dominant wavelength	2.5 mm

scales in the numerical experiment. Figure 20 shows the mean number of encounters n with scatterers for the particles that cross the receiver line as a function of time t. A least-squares fit of the line in figure 20 gives the mean time between consecutive encounters with scatterers, this can be used to infer that the mean free path l is given by $l = 15.56mm$. This quantity is much less than the size of the scattering region ($80mm$), which implies that the particles are strongly scattered.

For the scattering of waves, the scattering theory for isotropic point scatterers of section 4.1 is used. The wave-field for both the forward and reverse propagation is computed with equations (12) and (13). The wave propagation can only be invariant for time-reversal when energy is conserved. It is thus crucial that the scattering coefficients satisfy the optical theorem given in equation (16). The wavefield recorded by a receiver in the middle of the receiver array is shown in figure 21. The wave-field has the same character as the seismogram shown in the middle panel of figure 1; the direct wave merges with a coda of strongly scattered waves. This reflects the fact that for the employed parameter setting strong multiple scattering is operative.

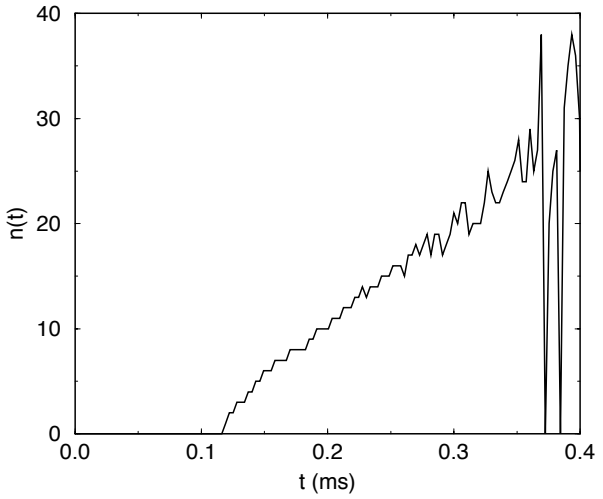

Figure 20. Mean number of scatterers encountered by particles as a function of the arrival time at the receiver line.

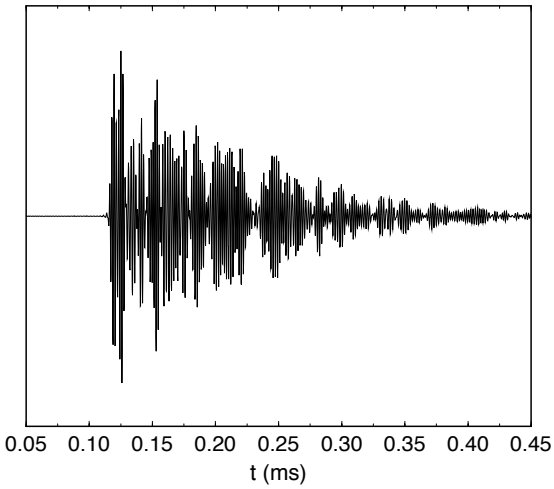

Figure 21. Wave-field at a receiver located in the middle of the receiver array.

TRI of the waves is carried out by recording the wave-field at 96 equidistant receivers on the receiver line, and by using the complex conjugate of the wave-field in the frequency domain as source signals that are emitted

from the receivers that now act as sources. An example of the wave-field after TRI is shown by the thick solid line in figure 22 where the time-reversed wave-field at time $t = 0$ is shown along the line $x = 0$. In the ideal case the wave-field focusses on the source at location $z = 0$. Due to the limited aperture of the receiver array and the finite bandwidth of the waves the focussing peak has a finite width and has sidelobes. For the TRI only the waves arriving between $0.25s$ and $0.30s$ have been used. It can be seen in figure 21 that this time window only contains multiple scattered waves in the coda.

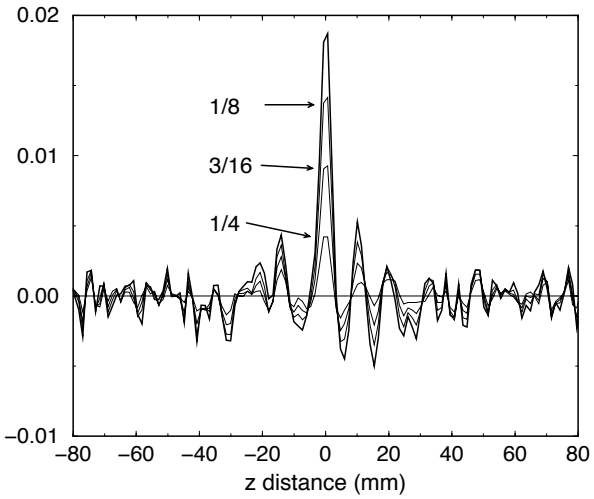

Figure 22. Time reversed wavefield at time $t = 0$ along the line $x = 0$. The source location is at $z = 0$. The thick solid lines is for TRI with the unperturbed receiver positions. The thin solid lines are for the wavefield after TRI with perturbed receiver positions. The numbers denote the rms value of the perturbation as a fraction of the dominant wavelength.

5.2. STABILITY ANALYSIS FOR SCATTERED PARTICLES

Consider the trajectories of a particle that is scattered with impact parameter b and with a perturbed impact parameter $b+\Delta$. The divergence of the trajectories is shown in figure 23. It follows from this figure and expression (28) that the divergence of the trajectories is given by $|\mathbf{r}_{b+\Delta}(t) - \mathbf{r}_b(t)| \approx vt\,(\Theta(b+\Delta) - \Theta(b)) = 2\pi vt\Delta/\sigma$. This implies that the error Δ_{out} at time t since the scattering is related to the initial error Δ_{in} by $\Delta_{out} = 2\pi\,(vt/\sigma)\,\Delta_{in}$.

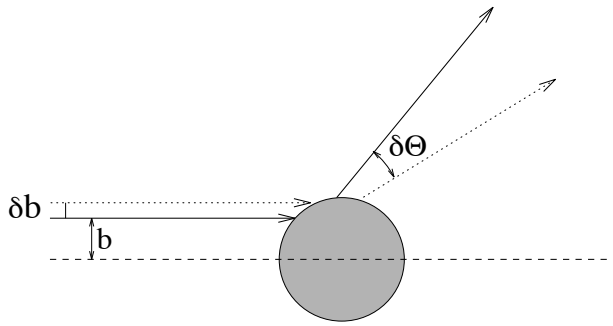

Figure 23. Divergence of the trajectories of the particles with impact parameter b and $b + \delta b$.

On average, vt is the mean-free path l, hence

$$\Delta_{out} = 2\pi\,(l/\sigma)\,\Delta_{in}\;. \tag{29}$$

When a wave is scattered n times, the error Δ_n follows by recursion:

$$\Delta_n = (2\pi l/\sigma)^n\,\Delta_0\;. \tag{30}$$

The number of scatterers encountered is on average given by $n = vt/l$, hence the Lyapunov exponent μ associated with the exponential divergence of trajectories is given by

$$\mu = \ln(2\pi l/\sigma)\;\; v/l\;. \tag{31}$$

Equation (30) gives the error in the trajectory after n scattering encounters. The error δ in the TRI is given by $\delta = D\,(\Delta\Theta) = D(d\Theta/db)\Delta_n$, where the distance D is defined in figure 18. Hence with (30) it follows that

$$\delta = \frac{2\pi D}{\sigma}\left(\frac{2\pi l}{\sigma}\right)^n \Delta_0\;. \tag{32}$$

When the error in the trajectory is of the order of $\sigma/2$ the trajectory will be completely different because the particle then encounters different scatterers. The associated critical perturbation δ_c follows from (30):

$$\delta_c = \left(\frac{\sigma}{2\pi l}\right)^n \frac{\sigma}{2}\;. \tag{33}$$

Using expression (31) for the Lyapunov exponent and using the relation $n = vt/l$ to eliminate n one finds that this critical length scale decreases exponentially with time:

$$\delta_c = \frac{\sigma}{2}\,e^{-\mu t}\;. \tag{34}$$

For the numerical experiments the critical length scale is shown in table 2. Also indicated is the precision with which the numerical simulations have been carried out. (All calculations were done in 64 bit arithmetic on an SGI Power Challenge.) Since the mean free path l is much larger than the scattering cross-section σ (table 1) the critical length scale decreases dramatically with the number of scattering encounters.

TABLE 2. Critical error δ_c for different numbers of scattering encounters. Also indicated is the employed machine precision.

n	$\delta_c(mm)$
1	0.0129
2	2.11×10^{-4}
3	3.43×10^{-6}
4	5.60×10^{-8}
5	9.11×10^{-10}
6	1.48×10^{-11}
7	2.41×10^{-13}
8	3.93×10^{-15}
Machine precision	0.22×10^{-15}
9	6.41×10^{-17}

The previous analysis applies for a perturbation of the starting point of a particle. When the scatterer locations are perturbed over a distance δ, a term δ should be added to the right-hand side of (29). The error after n scattering encounters is then given by

$$\Delta_n = \left(\frac{\left(\frac{2\pi l}{\sigma}\right)^{n+1} - 1}{\left(\frac{2\pi l}{\sigma}\right) - 1} \right) \Delta_0 \, . \tag{35}$$

However, given the high numerical value of $2\pi l/\sigma$ (≈ 61) in the numerical experiments this result is similar to (30) for the perturbation of initial conditions. The associated critical length scale is shown in table 3.

It follows that for the particles the critical length scale depends on the scattering cross section and the mean free path, and that this quantity depends exponentially on the number of scattering encounters (and thus on time). Due to this dependence the critical length scale δ_c is dramatically smaller than the scattering cross section σ.

TABLE 3. Critical length scales δ_c for different perturbations.

	Scatterer location	Source location
Particles	$\frac{1}{2}\left(\frac{\left(\frac{2\pi l}{\sigma}\right)-1}{\left(\frac{2\pi l}{\sigma}\right)^{n+1}-1}\right)\sigma$	$\frac{1}{2}\left(\frac{\sigma}{2\pi l}\right)^{n}\sigma$
Ballistic wave	$\frac{\sqrt{\lambda L}}{\sqrt{12(n+1)}}$	$\frac{\lambda}{4}$
Coda wave	$\frac{1}{\sqrt{2n}}\frac{\lambda}{4}$	$\frac{\lambda}{4}$

5.3. STABILITY ANALYSIS FOR SCATTERED WAVES

A fundamental difference between time reversed imaging of waves and particles is that TRI of particles occurs because a trajectory returns to the source at $t = 0$ whereas for waves TRI is achieved because the waves interfere at $t = 0$ constructively only near the source. The Feynman path summation given in expression (19) provides the basis for quantifying when the interference process that leads to TRI of waves is destroyed by the perturbations. When either the sources or the scatterers are perturbed for the waves, the dominant effect on the wave-field is the perturbation of the path length L_P in (19). When the variance σ_L of the path length is of the order of a quarter wavelength the resulting interference pattern is destroyed. Hence TRI of waves will break down when $\sigma_L \approx \lambda/4$.

The effect of the perturbation in the i-th component of the position vector of scatterer j on the path length L_P follows from the derivative

$$\frac{\partial L_P}{\partial x_i^{(j)}} = \frac{x_i^{(j)} - x_i^{(j-1)}}{\left|\mathbf{r}^{(j)} - \mathbf{r}^{(j-1)}\right|} - \frac{x_i^{(j+1)} - x_i^{(j)}}{\left|\mathbf{r}^{(j+1)} - \mathbf{r}^{(j)}\right|}\,, \tag{36}$$

which implies that

$$\sum_i \left(\frac{\partial L_P}{\partial x_i^{(j)}}\right)^2 = 2 - 2\frac{\left(\mathbf{r}^{(j)} - \mathbf{r}^{(j-1)}\right)\cdot\left(\mathbf{r}^{(j+1)} - \mathbf{r}^{(j)}\right)}{\left|\mathbf{r}^{(j)} - \mathbf{r}^{(j-1)}\right|\left|\mathbf{r}^{(j+1)} - \mathbf{r}^{(j)}\right|} = 2\left(1 - \cos\Theta_j\right)\,, \tag{37}$$

where Θ_j is the scattering angle at scatterer j. This angle is related to the angle φ_j in figure 30 by the relation $\Theta_j = \varphi_j - \varphi_{j-1}$. When the perturbations

of the locations of different scatterers are independent, the total variance in the path length is thus given by

$$\sigma_L^2 = \sum_j 2\,(1 - \cos\Theta_j)\,\delta^2\,, \tag{38}$$

where δ is the variance in the x and z coordinates of the scatterers.

For the coda the cosine of the scattering angle has zero mean because all scattering angles are equally likely: $\langle \cos\Theta_j \rangle = 0$. Using this, it follows from (38) that the variance in the path length joining n scatterers is given by

$$\sigma_L^{coda} = \sqrt{2n}\,\delta\,. \tag{39}$$

TRI of the coda breaks down when this quantity equals $\lambda/4$. The critical length scale for perturbations of the scatterer locations is thus given by

$$\delta_c^{coda} = \lambda / \left(4\sqrt{2n}\right)\,, \tag{40}$$

see Table 3. Note that in contrast to the situation for particles this critical length scale does not depend exponentially on n. Using the fact that the number of encountered scatterers increases linearly with time ($n = vt/l$) one finds that the critical length scale for the coda waves varies with time as $\delta_c^{coda} \sim 1/\sqrt{t}$. This time-dependence of the critical length scale for the coda waves is in stark contrast with the exponential decrease of the critical length scale for the particles with time given in (34). The $1/\sqrt{t}$ time-dependence of the critical length scale was also obtained by *Ballentine and Zibin* [1996] who show that for a periodically kicked rotator with a kick-strength that leads to classical solutions that are chaotic, the critical rotation angle $\delta\theta_{1/2}$ varies with time as $1/\sqrt{t}$ for large time.

For the ballistic wave (the wave that propagates along the line of sight from source to receiver) only forward scattering is of relevance. For forward scattering the term $(1 - \cos\Theta_j) \approx \Theta_j^2/2$ is small because the scattering angle is small. This leads to a reduction of the variance with a factor λ/L. The detailed analysis in appendix B shows that

$$\sigma_L^{ball} \approx \sqrt{\frac{3(n+1)}{4}}\sqrt{\frac{\lambda}{L}}\,\delta\,. \tag{41}$$

When σ_L^{ball} is about a quarter wavelength the interference is destroyed, hence the critical length scale is given by

$$\delta_c^{ball} \approx \sqrt{\lambda L}/\sqrt{12(n+1)}\,, \tag{42}$$

(see Table 3). Note that this length scale is proportional to the width $L_F = \sqrt{\lambda L/8}$ of the first Fresnel zone given in equation (1); when a scatterer is

moved over the width of the Fresnel zone it contributes in a fundamentally different way to the ballistic wave.

This is consistent with the theory of section 4.3 where it was argued that only the average scattering properties over the Fresnel zone affect the ballistic wave. The ballistic wave is only affected by the perturbation when a scatterer is moved out off the Fresnel zone or when a new scatterer is moved into the Fresnel zone. The relevant length scale for the ballistic wave thus is the width of the Fresnel zone rather than the wavelength, see expression (1).

When the source locations are perturbed over a distance δ but the scatterers remain fixed, only the length of the trajectory to the first scatterer is perturbed. This means that for this perturbation for both the coda and the ballistic wave $\sigma_L = \delta$. Thus, the critical length scale for perturbation of the source locations for both the coda and the ballistic wave is given by $\delta_c^{source} = \lambda/4$, see table 3.

5.4. NUMERICAL SIMULATIONS

In the TRI of particles 20,000 particles are propagated from the source to the receiver line and after time-reversal back-propagated to the source. For the case when the receivers and the scatterers are not perturbed, the only relevant error is the error in the numerical calculations. It follows from table 2 that with the employed machine precision particles with more than 8 scattering encounters will not be focused on the source during TRI. The numerical experiments confirm this conclusion. In the top panel of figure 24 the particles that have had 6 or fewer scatterer encounters are shown after TRI at time $t = 0$. In the ideal case all particles should be imaged at the source at $x = z = 0$. This is indeed the case, several thousand particles are imaged at the source, and only a few particles are far from the source position. The location of the particles that have had between 7 and 9 scatterer encounters is shown after TRI in the middle panel of figure 24. One can observe a clustering of particles near the source position, but the imaging is clearly degraded. The imaging further degrades for the particles that have encountered 10 or more scatterers, see the bottom panel of figure 24. In that case most particles are far from the source location. figure 24 confirms the analytical estimates of table 2 that with the employed numerical precision, 8 scatterer encounters mark the transition from accurate TRI to the loss of accuracy in the propagation of particles.

The quality of the time-reversed-image is quantified by $\exp(-error/D)$, where *error* denotes the mean distance of the particles to the source at $t = 0$. This imaging quality is shown in figure 25 as a function of the error in the source position for various values of the scattering encounter n. (The

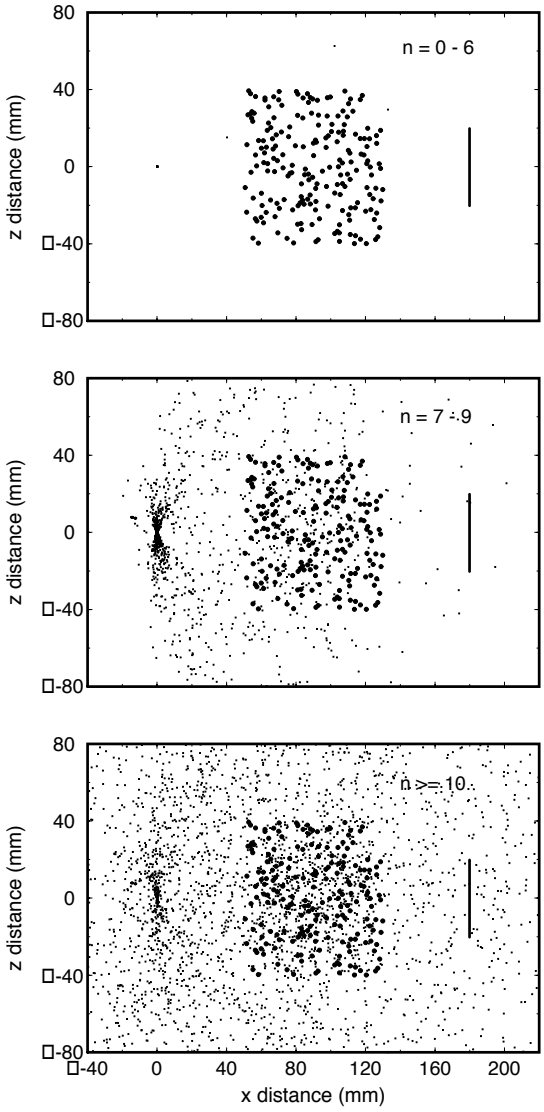

Figure 24. Locations of the particles (thin dots) at $t = 0$ after TRI for particles that have had 6 or less scattering encounters (top panel), between 7 and 9 scattering encounters (middle panel) and 10 or more scattering encountes (bottom panel). In the top panel several thousand particles are imaged on the source position at $x = z = 0$.

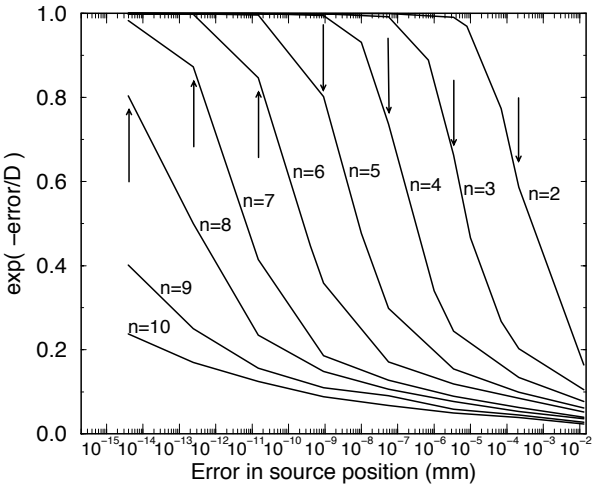

Figure 25. Imaging quality defined as $exp(-error/D)$ as a function of the perturbation of the initial position of the time reversed particle. The analytical stimates of the the critical perturbation are indicated by vertical arrows.

source position refers here to the receivers for the forward propagation that acts as sources for the time-reversed propagation.) The critical length scale shown in table 2 is indicated with the vertical arrows. The horizontal scale ends at the left with the machine precision. When the TRI degrades, the imaging quality decays from unity to zero, it follows from figure 25 that the analytical estimates of section 5.2 agree well with the numerical results. When the scatterer locations are perturbed rather than the source locations, the results are virtually the same. This is due to the fact that for large values of $2\pi l/\sigma$ the expressions (30) and (35) are almost identical.

TABLE 4. Time windows used in the different numerical experiments with waves and number of scattering encounters.

Wave	Time window (s)	Number of encounters
Ballistic	0.11-0.13	2
Coda 1	0.20-0.25	13
Coda 2	0.30-0.35	22
Coda 3	0.40-0.45	32

For the waves, TRI has been carried out for several time windows, see table 4. The imaged section along the line $z = 0$ of figure 18 is shown in figure 22 by the thick solid line. In this example, a short time window of the coda from $0.25s$ to $0.30s$ has been used. This section compares favorably with the experimental results of *Derode et al.* [1995]. The thin lines in figure 22 give the imaged section for various values of the perturbation in the position of the receivers that act as sources in the TRI; the number indicates the variance in the perturbation of the source location measured in wavelengths. It can be seen that TRI indeed breaks down when the source locations are perturbed over about a quarter wavelength. The quality of the TRI can be quantified by computing the ratio of the amplitudes of the imaging peak of TRI with perturbation to the imaging peaks without perturbation.

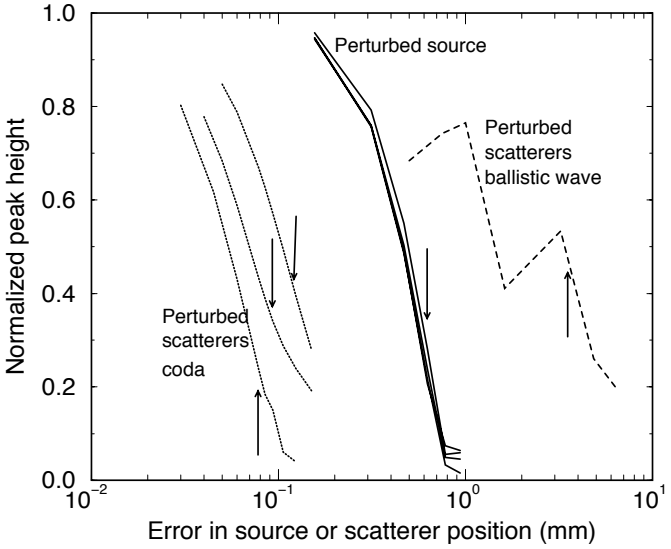

Figure 26. Quality of TRI of waves measured as the ratio of the peak height of the imaged section for the experiment with perturbed conditions compared to the peak height for the unperturbed imaged section. The dashed line represents the ballistic wave with perturbed scatterers. The dotted lines on the left are for the three coda intervals for peturbed scatterers with the latest coda interval on the left. The critical length scales from the theory are shown by vertical arrows.

The resulting relative peak heights are shown in figure 26 as a function of the error in source or scatterer locations for TRI experiments with the time windows shown in table 4. The critical length scales shown in table 3 are for each case indicated by vertical arrows. The curves for the

perturbation of the source position are the four solid lines in the middle. These curves are identical for the four employed time windows and show a decay when the perturbation is of the order $\lambda/4$ (which has the numerical value $0.625mm$). For the perturbation of scatterers for TRI of the ballistic wave, the critical length scale is significantly larger, and agrees will with the critical length scale shown in table 3. For TRI of the waves in the three coda intervals the critical length scale is appreciably less than a wavelength. The reason is that the number of scattering encounters is large for these waves, see table 4. The agreement between numerical simulations and the estimates shown in table 3 is very good. This confirms the assumption that the dominant effect of the perturbation of the time reversed imaging of waves is the perturbation of the path length.

5.5. WHY DO WAVES AND PARTICLES BEHAVE DIFFERENT?

It follows from the TRI of particles and waves that the stability of particle and wave motion for the perturbation of initial conditions or scatterer locations is fundamentally different. In the numerical experiments particles that have encountered 8 or more scatterers do not return to the source after TRI, whereas waves in the coda that have encountered up to at least 30 scatterers (table 4) focus well on the source after TRI.

The physical reason for this difference is that *particles* follow a single trajectory. When the initial condition of a particle or a scatterer along the trajectory are perturbed, the whole trajectory is perturbed, often in a dramatic fashion. Because of the chaotic nature of trajectories, the critical length scale is significantly less than the scattering cross-section by a factor that depends exponentially on the number of encountered scatterers and hence *exponentially* on time ($e^{-\mu t}$). This pertains both to the perturbation of the source position as well as to the perturbation of the scatterer position.

For the *waves* when the source or scatterer location is perturbed, the different wave-paths are not perturbed fundamentally; only the length of the wave-paths is changed. However, this perturbation only leads to appreciable effects when this perturbation is approximately a quarter-wavelength, because it is the interference of the waves along all possible wave-paths that determines the total wave-field. For both the coda and the ballistic wave the critical perturbation of the source location is a quarter-wavelength. For the perturbation of the scatterers the critical length-scale for the coda is proportional to the wavelength, but much smaller with a factor $1/\sqrt{2n}$. In contrast, the ballistic wave is only sensitive to perturbations of the scatterer position that are of the order of the width of the Fresnel zone. Since the number of scatterers encountered increases linearly with time, the critical length scale varies with time as $1/\sqrt{t}$ rather than the exponential time-

dependence for the ciritical length scale for particles.

This implies that waves and particles react in fundamentally different ways to perturbations of the initial conditions or of the medium. The reason for this is that particles "select" a certain trajectory whereas waves travel along all possible trajectories visiting all the scatterers in all possible combinations. It is the "selection process" of a particle trajectory that creates the fundamentally larger instability of particle propagation than of wave propagation.

6. Discussion, imaging in complex media?

Imaging can only be carried out when the medium is known reasonably well because one needs to know the position of the waves in order to determine where the image is created. In general, imaging is achieved by an interference process. When a medium without scatterers is used as a reference model for an imaging experiment, then the medium must be known with such an accuracy that the error in the location of the wavefronts is less than $\lambda/4$. A larger error will destroy the interference process through which the imaging is achieved.

As shown in section 5.3, when multiple scattered waves are used for to carry out imaging the scatterer locations must be known with an error less than $(\lambda/4)/\sqrt{2n}$, where n is the number of scatterers encountered along the path. This suggest that multiple scattering does not fundamentally change the requirements that the medium needs to satisfy for successful imaging. The only change is the additional factor $1/\sqrt{2n}$ in the required precision, which suggest a quantitative difference in the required accuracy rather than a qualitative difference. Given the fact that the number of scatterer encounters n can be quite large this quantitative difference can be significant.

However, there is a more important qualitative issue at stake. When one carries out imaging in a medium without scatterers, one needs to know the location of the *wavefronts* within an accuracy $\lambda/4$. As shown in the sections 3.2 and 4.3, the location of the wavefronts depends predominantly on the average properties of the medium over the Fresnel zone. This means that a detailed knowledge of the medium is not needed, as long as the properties averaged over the Fresnel zone are known. In contrast to this, for imaging with multiple scattered waves the location of the *scatterers* must be known with an accuracy $(\lambda/4)/\sqrt{2n}$. It is for this reason that multiple scattered waves often are not used in imaging experiments where the medium is known with only limited precision.

However, the requirements for imaging with waves are favorable compared to the requirements for imaging with particles. There are two reasons

for this:

[1] Waves travel along *all* possible trajectories, and remain doing this when the scatterers are perturbed. In contrast to this, particle travel along a *single* trajectory. As shown in the sections 5.4 and 5.5 this makes the propagation of particles fundamentally more sensitive to perturbations of the scatterers than the propagation of waves.

[2] For the ballistic wave the wave-field depends only on the average properties of the medium over the Fresnel zone, see the sections 3.2 and 4.3. The averaging carried out by the wave-field obviates the need for a detailed description of the structure within the Fresnel zone. There is no counterpart of this averaging property for particles.

Both factors are favorable for the stability of wave propagation compared to particle propagation in strongly scattering media. This is not only of importance for the possibility (or impossibility) of imaging experiments, but this difference should also be a crucial element in the comparison between classical chaos and quantum chaos.

Acknowledgments: I thank Peggy Hellweg, Axel Roehm and Osamu Nishizawa for providing figures. Numerous discussions with John Scales have been invaluable for the work on wave and particle chaos. Mathias Fink is thanked for making me aware of the robustness of time-reversed imaging in the presence of strong scattering.

A. The nonlinear scattering coefficient of a single scatterer

As a simple prototype of a system that exhibits multiple scattering by a single scatterer consider a delta function scatterer with strength g in one dimension:

$$L^{(0)}u(x) = g\delta(x)u(x) \ . \tag{43}$$

The operator $L^{(0)}$ characterizes the dynamics of the unperturbed system. For the Schrödinger equation this operator is given by $L^{(0)} = \nabla^2 + k^2$. Let the solution in the absence of the scatterer be denoted by $u^{(0)}$. The field then satisfies the Lippmann-Schwinger equation

$$u(x) = u^{(0)}(x) + \int G(x,x')g\delta(x')u(x')dx' \ , \tag{44}$$

which is equivalent to

$$u(x) = u^{(0)}(x) + G(x,0)gu(0) \ . \tag{45}$$

This expression appears to be the same as equation (12) for the special case of a single scatterer. However, one cannot make this comparison because the wave-field u_j in (12) denotes the waves that are incident on the scatterer while $u(0)$ denotes the *total* wave-field at the scatterer.

These equations can be reconciled by setting $x = 0$ in (45), which gives: $u(0) = u^{(0)}(0) + G(x,0)gu(0)$. The wave-field at the scatterer can be obtained from this result and is given by

$$u(0) = \frac{1}{1 - gG(0,0)} u^{(0)}(0) \tag{46}$$

Inserting $u(0)$ in the right hand side of (45) then gives

$$u(x) = u^{(0)}(x) + G(x,0)\frac{g}{1 - gG(0,0)} u^{(0)}(0) \; . \tag{47}$$

This expression can be compared with equation (12) for the special case of one scatterer because the incident wave-field is given by $u^{(0)}$. Note that the scattering coefficient $g/(1 - gG(0,0))$ depends nonlinearly on the scattering strength g.

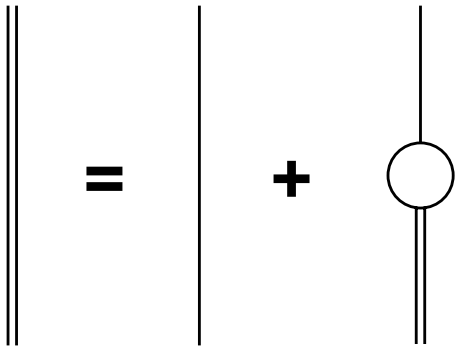

Figure 27. Diagrammatic representation of the wave-field $u = u^{(0)} + Ggu$. The single line denotes the unperturbed wave $u^{(0)}$ and G, the double line denotes the perturbed wave u and the open circle denotes the linear scattering coefficient g.

The scattering process can thus be described by the two alternative representations (45) and (47). These representations are shown graphically in the figures 27 and 28 respectively. In these figures a single line denotes the unperturbed wave-field and the double line the perturbed wave-field. The single scattering interaction g is denoted with an open circle while the nonlinear scattering coefficient $g/(1 - gG(0,0))$ is shown with a black circle.

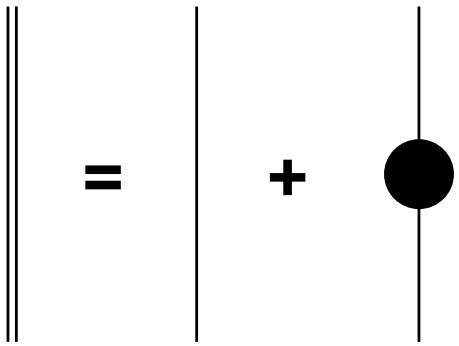

Figure 28. Alternative diagrammatic representation of the wave-field $u = u^{(0)} + G(1 - gG)^{-1}gu^{(0)}$. The single line denotes the unperturbed wave $u^{(0)}$ and G, the black circle denotes the nonlinear scattering coefficient $(1 - gG)^{-1}g$.

It is instructive to consider the following expansion of the nonlinear scattering coefficient:

$$\frac{g}{1 - gG} = g + gGg + gGgGg + \cdots \tag{48}$$

This expression is graphically represented in figure 29. The series expresses the full nonlinear scattering coefficient as a single scattering interaction, plus a repeated double scattering interaction at the same scatterer plus all higher order repeated scattering interactions with the same scatterer. The nonlinear scattering coefficient thus accounts for all consecutive scattering encounter with the same scatterer.

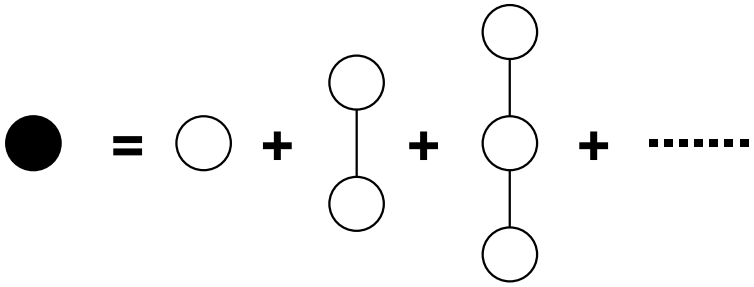

Figure 29. Diagrammatic representation of the nonlinear scattering coefficient. The single line denotes the unperturbed Green's function $G(0, 0)$. The open circle denotes the scattering g and the black circle stands for the nonlinear scattering coefficient.

The equations shown here break down for wave-propagation problems in more dimensions because the Green's function $G(0, 0)$ is singular in that case. This complication can, however, be remedied [*Nieuwenhuizen et al.*,

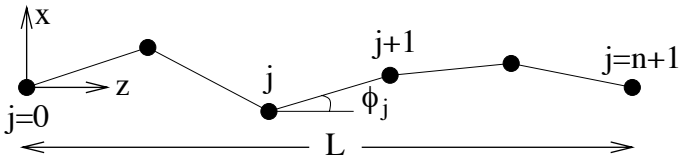

Figure 30. Geometry of the path of the scattered ballistic wave.

1992; *de Vries et al.*, 1998]. However, for any linear system in any dimension, the scattered waves are related linearly to the incident wave-field. This is the only condition that is used in expression (12). The scattering coefficient are in general related in a nonlinear way to the perturbation that causes the scattering.

As an example one can consider scattering of acoustic waves by a spherical scatterer with a perturbed bulk modulus with a radius much smaller than a wavelength. As shown in *Morse and Ingard* [1968] the scattering is isotropic and the scattered waves depend linearly on the incident waves. Thus the conditions required for equation (12) are satisfied for this system.

B. The variance in the path length for the ballistic wave

For small scattering angles Θ_j the variance in the path length given in (38) reduces to

$$\sigma_L^2 = \sum_{j=1}^{n} \left\langle \Theta_j^2 \right\rangle \delta^2 \,. \tag{49}$$

As a simplified model for the ballistic wave we assume that n scatterers are separated with the same spacing Δ along the source-receiver path, this separation is given by

$$\Delta = \frac{L}{(n+1)} \,, \tag{50}$$

see figure 30. The fixed positions of the source and receiver are denoted by (x_0, z_0) and (x_{n+1}, z_{n+1}) respectively, hence $x_0 = x_{n+1} = 0$. The positions of the scatterers are prescribed by the distance x_j from the source-receiver line, the angle between the path from scatterer j to scatterer $j+1$ is denoted by φ_j. Since this angle is small $\varphi_j = (x_{j+1} - x_j)/\Delta$, so that the scattering angle is given by

$$\Theta_j = \varphi_j - \varphi_{j-1} = (x_{j+1} - 2x_j + x_{j-1})/\Delta \,. \tag{51}$$

The variance in the path length follows by inserting (51) in (49). The cross-terms that appear vanish on average because the positions of the scatterers are independent: $\langle x_{j+1} x_j \rangle = 0$. When all the scatterers have

the same rms distance $\langle x^2 \rangle$ to the source-receiver line (with the exception of the terms $j = 0$ and $j = n+1$ for which $x_0 = x_{n+1} = 0$) it follows that $\sigma_L^2 = (6n-2)\langle x^2 \rangle \delta^2/\Delta$. Given the crudeness of the scattering model, the factor -2 in this expression is ignored so that the scattering angle is approximately equal to

$$\sigma_L^2 = \frac{6\delta^2}{\Delta^2} n \left\langle x^2 \right\rangle \tag{52}$$

The rms distance $\langle x^2 \rangle$ is at this point unknown, this quantity follows from the requirement that the scatterers are located within the first Fresnel zone. The length L_j of the path from scatterer j to scatterer $j+1$ is given by $L_j = \sqrt{\Delta^2 + (x_{j+1} - x_j)^2} \approx \Delta + (x_{j+1} - x_j)^2 / 2\Delta$. The detour d of the scattered wave compared to the direct wave is thus given by:

$$d = \sum_{j=0}^{n} L_j - L = \frac{1}{2\Delta} \sum_{j=0}^{n} (x_{j+1} - x_j)^2 \tag{53}$$

Using the fact that the scatterer positions are uncorrelated one finds with $x_0 = x_{n+1} = 0$ that on average

$$\langle d \rangle = \frac{n \langle x^2 \rangle}{\Delta} \, . \tag{54}$$

The scatterers contribute to the ballistic wave when the detour is less than a quarter wavelength. Assuming that this corresponds to a mean detour $\langle d \rangle$ of $\lambda/8$ one finds the corresponding variance $\langle x^2 \rangle$ from (54):

$$n \left\langle x^2 \right\rangle = \frac{\lambda \Delta}{8} \, . \tag{55}$$

Using this in (52) and using (50) to eliminate Δ then gives the variance of the path length of the ballistic wave:

$$\sigma_L^{ball} = \sqrt{\frac{3(n+1)}{4}} \sqrt{\frac{\lambda}{L}} \, \delta \, . \tag{56}$$

References

1. Aki, K., and P.G. Richards, *Quantitative seismology*, Freeman Co, San Fransisco, 1980.
2. Alsina, D., R.L. Woodward, and R.K. Snieder, Shear-Wave Velocity Structure in North America from Large-Scale Waveform Inversions of Surface Waves, *J. Geophys. Res., 101*, 15969-15986, 1996.
3. Ballentine, L.E. and J.P. Zibin, Classical state sensitivity from quantum mechanics, *Phys. Rev. A, 54*, 3813-3819, 1996.

4. Bleistein, N., *Mathematical methods for wave phenomena*, Academic Press, Orlando, 1984.
5. Červený, V., and F. Hron, The ray series method and dynamical ray tracing system for three-dimensional inhomogeneous media, *Bull. Seismol. Soc. Am., 70*, 47-77, 1980.
6. Choy, G.L., and P.G. Richards, Pulse distortion and Hilbert transformation in multiply relfected and refracted body waves, *Bull. Seismol. Soc. Am., 65*, 55-70, 1975.
7. Claerbout, J.F., *Imaging the Earth's interior*, Blackwell, Oxford, 1985.
8. Dahlen, F.A., and J. Tromp, *Theoretical global seismology*, Princeton University Press, Princeton, 1998.
9. Derode, A., P. Roux, and M. Fink, Robust acoustic time reversal with high-order multiple scattering, *Phys. Rev. Lett., 75*, 4206-4209, 1995.
10. de Vries, P., D.V. van Coevoorden, and A. Lagendijk, Point scatterers for clasical waves, *Rev. Mod. Phys., 70*, 447-466, 1998.
11. Dolan, S.S., C.J. Bean, and B. Riollet, The broad-band fractal nature of heterogeneity in the upper crust from petrophysical logs, *Geophys. J. Int., 132*, 489-507, 1998.
12. Draeger, C., and M. Fink, One-channel time reversal of elastic waves in a chaotic 2D-silicon cavity, *Phys. Rev. Lett., 79*, 407-410, 1997.
13. Feynman, R.P., and A.R. Hibbs, *Quantum mechanics and path integrals*, McGraw-Hill, New York, 1965.
14. Fink, M., Time Reversed Acoustics, *Physics Today, 50(3)*, 34-40, 1997.
15. Groenenboom, J., and R. Snieder, Attenuation, dispersion and anisotropy by multiple scattering of transmitted waves through distributions of scatterers, *J. Acoust. Soc. Am., 98*, 3482-3492, 1995.
16. Gutzwiller, M.C., *Chaos in classical and quantum mechanics*, Springer Verlag, New York, 1990.
17. Herrmann, F., A scaling medium representation; a discussion on well-logs, fractals and waves, *PhD thesis, Delft University of Technology*, pp. 298, 1997.
18. Ishimaru, A., *Wave propagation and scattering in random media*, Oxford University Press, Oxford, 1997.
19. Iyer, H.M., and K. (Eds.) Hirahara, *Seismic tomography; theory and practice*, Chapman and Hall, London, 1993.
20. Kravtsov, Ya.A., Rays and caustics as physical objects, in *Prog. in Optics, XXVI*, edited by E. Wolf, 227-348, Elsevier, Amsterdam, 1988.
21. Lax, M., Multiple scattering of waves, *Rev. Mod. Phys., 23*, 287-310, 1951.
22. Lomax, A., and R. Snieder, Estimation of finite-frequency waveforms through wavelength-dependent averaging of velocity, *Geophys. J. Int., 126*, 369-381, 1996.
23. Longuet-Higgins, M.S., A theory for for the generation of microseisms, *Phil. Trans. R. Soc. London Ser. A, 243*, 1-35, 1950.
24. Marquering, H., G Nolet, and F.A. Dahlen, Three-dimensional waveform sensitivity kernels, *Geophys. J. Int., 132*, 521-534, 1998.
25. Morse, P., and H. Feshbach, *Methods of theoretical physics, Part 1*, McGraw-Hill, New York, 1953.
26. Morse, P.M., and K.U. Ingard, *Theorerical acoustics*, McGraw-Hill, New York, 1968.
27. Nayfeh, A.H., *Perturbation methods*, John Wiley and Sons, New York, 1973.
28. Neele, F., and R. Snieder, Are long-period body wave coda caused by lateral heterogeneity?, *Geoph. J. Int., 107*, 131-153, 1991.
29. Niewenhuizen, T.M., A. Lagendijk, and B.A. van Tiggelen, Resonant point scatterers in multiple scattering of classical waves, *Phys. Lett. A., 169*, 191-194, 1992.
30. Nishizawa, O., T. Satoh, Xinglin Lei, and Y. Kuwahara, Laboratory studies of seismic wave propagation in inhomogeneous media using a laser doppler vibrometer, *Bull. Seismol. Soc. Am., 87*, 809-823, 1997.
31. Rytov, S.M., Yu. A. Kravtsov, and V.I. Tatarskii, *Principles of statistical radiophysics 4; Wave propagation through random media*, Springer-Verlag, Berlin, 1989.

32. Scales, J., and R. Snieder, Humility and nonlinearity, *Geophysics, 62*, 1355-1358, 1997.
33. Scales, J., and R. Snieder, What is noise?, *Geophysics, 63*, 1122-1124, 1998.
34. Snieder, R., 3D Linearized scattering of surface waves and a formalism for surface wave holography, *Geophys. J. R. astron. Soc., 84*, 581-605, 1986.
35. Snieder, R., On the connection between ray theory and scattering theory for surface waves, in *Mathematical Geophysics, a survey of recent developments in seismology and geodynamics*, edited by Vlaar, N.J., Nolet, G., Wortel, M.J.R. and Cloetingh, S.A.P.L., 77-83, Reidel, Dordrecht, 1987.
36. Snieder, R., The optical theorem for surface waves and the relation with surface wave attenuation, *Geophys. J., 95*, 293-302, 1988.
37. Snieder, R., Global inversions using normal modes and long-period surface waves, in *Seismic tomography*, edited by H.M. Iyer and K. Hirahara, 23-63, Prentice-Hall, London, 1993.
38. Snieder, R., The evolution of phase fronts and the method of strained coordinates, *J. Acoust. Soc. Am., 103*, 3180-3183, 1998.
39. Snieder, R., and C. Chapman, The reciprocity properties of geometrical spreading, *Geophys. J. Int., 132*, 89-95, 1998.
40. Snieder, R., and A. Lomax, Wavefield smoothing and the effect of rough velocity perturbations on arrival times and amplitudes, *Geophys. J. Int., 125*, 796-812, 1996.
41. Snieder, R. and G. Nolet, Linearized scattering of surface waves on a spherical Earth, *J. Geophys., 61*, 55-63, 1987.
42. Snieder, R. and B. Romanowicz, A new formalism for the effect of lateral heterogeneity on normal modes and surface waves -I: Isotropic perturbations, perturbations of interfaces and gravitational perturbations *Geophys. J. R. astron. Soc., 92,* 207-222, 1988.
43. Snieder, R., and J.A. Scales, Time reversed imaging as a diagnostic of wave and particle chaos, *Phys. Rev. E, 58*, 5668-5675, 1998.
44. Tabor, M., *Chaos and integrability in nonlinear dynamics*, Wiley-Interscience, New York, 1989.
45. Tanimoto, T., A simple derivation of the formula to calculate synthetic long-period seismograms in a heterogeneous earth by normal mode summation, *Geophys. J.R. Astron. Soc., 77*, 275-278, 1984.
46. van der Hulst, H.C., On the attenuation of plane waves by obstacles of arbitrary size and form, *Physica, 15*, 740-746, 1949.
47. Waterman, P.C., and R. Truell, Multiple scattering of waves, *J. Math. Phys., 2*, 512-537, 1961.
48. Webb, S.C., Broadband seismology and noise under the ocean, *Rev. Geophys., 36*, 105-142, 1998.
49. Woodhouse J.H. and F.A. Dahlen, The effect of a general aspherical perturbation on the free oscillations of the Earth, *Geophys. J.R. astr. Soc., 53,* 335-354, 1978.
50. Yilmaz, O., Seismic data processing, *Investigations in geophysics, 2*, Society of Exploration Geophysicists, Tulsa, 1987.